Membrane Cholesterol Efflux Drives Tumor-Associated Macrophage Reprogramming and Tumor Progression

Pieter Goossens, Juan Rodriguez-Vita, Anders Etzerodt, Marion Massé, Olivia Rastoin, Victoire Gouirand, Thomas Ulas, Olympia Papantonopoulou, Miranda van Eck, Nathalie Auphan-Anezin, et al.

Total characters : 63,592

Membrane cholesterol efflux drives tumor-associated macrophage reprogramming and tumor progression.

Pieter Goossens[1,2,†], Juan Rodriguez-Vita[1,3,†], Anders Etzerodt[1,4], Marion Masse[1], Olivia Rastoin[1], Victoire Gouirand[1], Thomas Ulas[5,6], Olympia Papantonopoulou[5], Miranda Van Eck[7], Nathalie Auphan-Anezin[1], Magali Bebien[1], Christophe Verthuy[1], Thien Phong Vu Manh[1], Martin Turner[8], Marc Dalod[1], Joachim L. Schultze[5,6], Toby Lawrence[1,9,10,*]

1. Aix Marseille Univ, CNRS, INSERM, CIML, Marseille, 13009, France.

2. Department of Pathology, Cardiovascular Research Institute Maastricht, Maastricht University, 6229HX, The Netherlands.

3. Vascular Signaling and Cancer (A270), German Cancer Research Center (DKFZ), Heidelberg, 69120, Germany.

4. Department of Biomedicine, Aarhus University, Aarhus, 8000, Denmark

5. Genomics & Immunoregulation, Life and Medical Sciences Institute (LIMES), University of Bonn, Bonn, 53115, Germany.

6. PRECISE Platform for Single Cell Genomics and Epigenomics, German Center for Neurodegenerative Diseases and University of Bonn, Bonn, 53127, Germany

7. Division of BioTherapeutics, Leiden Academic Centre for Drug Research, Universiteit Leiden, 2300RA, The Netherlands.

8. Laboratory of Lymphocyte Signaling and Development, The Babraham Institute, Cambridge, CB22 3AT, UK.

9. Centre for Inflammation Biology and Cancer Immunology, School of Immunology & Micribial Sciences, King's College London, SE1 1UL, UK.

10. Xinxiang Medical University, Henan Province 453003, China.

† These authors contributed equally.

* Lead contact/Corresponding author: Prof. Toby Lawrence, Centre for Inflammation Biology and Cancer Immunology, School of Immunology & Micribial Sciences, King's College London, SE1 1UL, UK. Tel: +44(0)207 848 8630, Email: toby.lawrence@kcl.ac.uk.

Running title: Cholesterol efflux from TAM drives tumor progression

Summary

Macrophages possess intrinsic tumoricidal activity, and yet tumor-associated macrophages (TAMs) rapidly adopt an alternative phenotype within the tumor microenvironment that is marked by tumor-promoting immunosuppressive and trophic functions. The mechanisms that promote such TAM polarization remain poorly understood, but once identified they may represent important therapeutic targets to block the tumor-promoting functions of TAMs and restore their anti-tumor potential. Here we have characterized TAMs in a mouse model of metastatic ovarian cancer. We show that ovarian cancer cells promote membrane-cholesterol efflux and depletion of lipid rafts from macrophages. Increased cholesterol efflux promoted IL-4-mediated reprogramming, including inhibition of IFNγ-induced gene expression. Genetic deletion of ABC transporters, that mediate cholesterol efflux, reverts the tumor-promoting functions of TAMs and reduced tumor progression. These studies reveal an unexpected role for membrane-cholesterol efflux in driving TAM-mediated tumor progression, while pointing to a potentially novel anti-tumor therapeutic strategy.

Keywords

Tumor-associated macrophages, Ovarian cancer, Cholesterol efflux, Lipid rafts, IL-4 signaling

Introduction

There is now a wealth of clinical and experimental evidence that strongly links tumor-associated macrophages (TAMs) with tumor progression, invasion and metastasis (Noy and Pollard, 2014). In the vast majority of published studies, increased numbers of TAMs correlate with poor prognosis, but in some cases, specific TAM subsets have been associated with beneficial outcomes (de Vos van Steenwijk et al., 2013). Indeed, macrophages have been shown to posses intrinsic tumoricidal activity and promote the activation of cytotoxic lymphocytes (Hagemann et al., 2008), but they rapidly adopt an alternative phenotype within tumors, associated with immune-suppression and trophic functions that support tumor growth (Mantovani et al., 2008). However, the mechanisms that promote TAM reprogramming in the tumor-microenvironment remain poorly understood.

In mammals, macrophages are found in all tissues after birth and are endowed with trophic functions that contribute to organ development and remodelling (Pollard, 2009). Recent advances in genetic fate-mapping techniques have revealed that the majority of tissue-resident macrophages, at least in steady-state, develop from embryonic precursors and are maintained

by local proliferation with little input from hematopoeitc stem cells (HSC) in the bone marrow (Schulz et al., 2012). Subsequent studies have shown that embryonic macrophages can be gradually replaced by HSC-derived blood monocytes, to varying degrees depending on the specific context (Ginhoux and Guilliams, 2016). But the functional implications of these distinct developmental origins and certainly their respective contributions to tumor progression remain unclear. In a recent study, both tissue-resident macrophages of embryonic origin and monocyte-derived TAMs were shown to contribute towards tumor growth in a mouse model of pancreatic cancer (Zhu et al., 2017). The phenotype of tissue-resident macrophages is dictated by the tissue-specific signals in their respective niche (Lavin et al., 2014). Along these lines, TAMs in various experimental models and human cancers have been shown to express uniques sets of gene patterns including the production of specific chemokines, cytokines and growth factors linked with tumor progression, such as CCL2, TNF, VEGF, basic fibroblast growth factor (bFGF) and matrix metalloproteinases (MMPs) (Kratochvill et al., 2015). Thus, TAMs are reprogrammed towards a functional state that supports tumor growth and immune-suppression and away from inflammatory phenotypes that could be associated with anti-tumor functions. However, the specific mechanisms that drive TAM accumulation and polarization in different tumors remain unclear.

Here we have characterized TAMs in a mouse model of metastatic ovarian cancer. We show that monocyte-derived TAMs gradually replaced resident macrophages in this model and displayed an upregulation of cholesterol metabolism and reverse cholesterol efflux pathways during tumor progression. Further experiments revealed that ovarian cancer cells actively promoted plasma membrane cholesterol efflux from macrophages and the subsequent loss of cholesterol-rich membrane microdomains, or so called “lipid rafts”. Increased cholesterol efflux promoted enhanced IL-4 signaling in macrophages while inhibiting IFNγ-induced gene expression. As previously reported, IL-4-induced gene expression in TAMs is associated with tumor-promoting functions, including increased arginine metabolism promoting immune-suppression and trophic functions, supporting invasion and metastasis (DeNardo et al., 2009). Whereas, IFNγ induced gene expression in TAMs drives anti-tumor functions. We further demonstrate that IL-4 signaling and cholesterol efflux pathways in TAMs significantly contribute to tumor progression *in vivo*. Furthermore, genetic deletion of ABC transporters reverts the tumor-promoting functions of TAMs. These studies suggest an important role for membrane-cholesterol efflux in driving IL-4 signaling and tumor-promoting functions of TAMs in ovarian cancer, while rendering them refractory to reprogramming by anti-tumor cytokines. Therefore, preventing cholesterol efflux in TAMs could represent a novel therapeutic strategy to block their pro-tumor functions and restore anti-tumor immunity.

Results

Origins of TAMs during ID8 tumor development.

High grade serous ovarian cancer (HGSC) is frequently associated with colonisation of the peritoneal cavity by cancer cells (George et al., 2016). ID8 cells are spontaneously transformed mouse ovarian surface epithelial cells (Urzua et al., 2016), when adoptively transferred by intra-peritoneal (i.p.) injection in syngeneic mice, these cells progressively develop a malignant ascites with tumor nodules throughout the peritoneal cavity (Hagemann et al., 2008), which is characteristic of HGSC. The peritoneal cavity is populated by two major subsets of serosal macrophages; large peritoneal macrophages (LPM), which are most abundant, and a minor population of small peritoneal macrophages (SPM) (Ghosn et al., 2010). Previous studies have shown that SPM and LPM have distinct developmental origins; SPM develop from blood monocytes which are derived from bone marrow progenitors, whereas LPM are derived from embryonic progenitors and are maintained independently of blood monocytes, retaining proliferative capacity for self-renewal (Yona et al., 2013). More recent studies have shown that LPM can be progressively replaced by long-lived bone marrow-derived macrophages that maintain self-renewal potential (Bain et al., 2016). To monitor the dynamics of peritoneal macrophages (PM) during ID8 tumor growth, we first characterized macrophage subsets by flow cytometry. SPM and LPM can be distinguished by F4/80 and MHCII expression; SPM are MHCII^{hi} F4/80^{lo} whereas LPM are F4/80^{hi} MHCII^{lo} (Fig.1A). LPM represent approximately 80 % of PM in naïve mice, however, after seeding of ID8 cells in the peritoneal cavity, a significant population of F4/80^{int} MHCII^{int} PM rapidly accumulates (intPM; Fig.1A). Kinetic analysis of total cell numbers revealed that LPM numbers remain relatively constant throughout tumor progression, while intPM progressively accumulate and eventually become the dominant TAM population (Fig.1B).

To determine the dynamics of PM subsets during ID8 tumor growth, we performed fate-mapping studies with shielded radiation chimera mice. Radiation chimeras can be used to determine the contribution of bone marrow-derived progenitors towards cells in a given tissue. However, irradiation kills tissue-resident macrophages that then become replaced by monocyte-derived cells, thus to distinguish tissue-resident cells from monocyte-derived macrophages from the bone marrow, it is necessary to protect the tissue from the effects of radiation using lead shielding. To study the origins of PM subsets during ID8 tumor growth, we shielded the abdomen of host C57BL6 CD45.1 congenic mice during irradiation and then adoptively transferred a mixture of bone marrow cells from mice expressing both CD45.1 and CD45.2 (CD45.1/2) and *Ccr2*$^{-/-}$ mice, expressing only CD45.2. This allowed the distinction

between host (CD45.1) and donor cells (CD45.1/2 or CD45.2), as well as their CCR2-dependency, CD45.2 single-positive cells being CCR2-dependent. Due to the low engraftment efficiency of *Ccr2*$^{-/-}$ bone marrow cells, *Ccr2*$^{-/-}$ donor cells were mixed at a ratio of 4:1 with competitor B6.CD45.1/2 cells. Five weeks after bone marrow engraftment, chimeric mice were injected with ID8 cells to track the contribution of bone marrow-derived cells to PM subsets (Fig.1C). CD45.1 and CD45.2 expression in TAM subsets was measured by flow cytometry a further 8 weeks after injection of ID8 cells, a total of 13 weeks after adoptive transfer of bone marrow cells, chimerism was normalised to blood monocytes. These experiments revealed that SPM and intPM were derived from CCR2-dependent bone marrow progenitors, with almost 100 % chimerism after 8 weeks of tumor growth (Fig.1D,E). However, at this time point, LPM only showed approximately 30 % chimerism, implying that LPM are more gradually replaced by bone marrow-derived cells during tumor development. To confirm the CCR2-dependency of intPM, we analyzed the accumulation of PM subsets in full CCR2 deficient mice (*Ccr2*$^{-/-}$), as expected, both SPM and intPM were drastically reduced in *Ccr2*$^{-/-}$ mice bearing ID8 tumors, whereas CCR2 deficiency had little impact on LPM numbers (Fig.S1).

To confirm the continuous contribution of blood monocytes to SPM and intPM populations throughout tumor growth, we used a fluorescent fate-mapping approach. The chemokine receptor Cx3cr1 is expressed by blood monocytes (Geissmann et al., 2003) and previous studies have demonstrated the fate-mapping of monocyte-derived cells using knock-in mice that express a tamoxifen-inducible Cre-recombinase from the Cx3cr1 locus (*Cx3cr1*^{CreER}), crossed to mice expressing a ubiquitous lox-STOP-lox reporter cassette (Yona et al., 2013). As expected, we did not detect Cx3cr1 expression in steady-state LPM using the *Cx3cr1*$^{egfp/+}$ reporter mice, however, high levels of Cx3cr1 expression were observed in SPM and intermediated levels in intPM (Fig.S1), reflecting the likely monocyte origins of these cells. We crossed *Cx3cr1*^{CreER} mice with Rosa26-lsl-tdRFP reporter mice (*Cx3cr1*^{CreER}:R26-tdRFP) and injected these mice with ID8 cells to track monocyte-derived cells during tumor growth. Six weeks after injection of ID8 cells, mice were given a single dose of 4-OHT by oral gavage (p.o.) and RFP expression in TAM subsets was measured by flow cytometry ten days later. These experiments showed strong RFP labelling in SPM and intPM within 10 days of 4-OHT administration, with very little labelling of LPM (Fig.1F,G). These data clearly demonstrated the contribution of blood monocytes to SPM and intPM during tumor growth, even within this short time frame.

Transcriptional profiling of TAMs

To evaluate the impact of the tumor-microenvironment on PM phenotype, we performed global gene expression analysis using microarrays on bulk PM from naïve mice and at different time

points during tumor progression. We isolated naïve F4/80^{hi} PM and TAMs at 5, 12 and 21 days during ID8 tumor development by flow cytometry (Fig.S2). Total RNA was extracted and samples were analyzed using MoGene 1.0st microarrays. RMA normalised data were filtered and analyzed for variations in gene expression. The heatmap in figure S2B shows the 1000 most variable genes in the dataset. To extract differentially expressed genes (DEGs) between naïve PM and TAMs at the different time points, we used Anova with an adjusted p value and a threshold of 1.5 fold change (FC). We then used Gene Ontology (GO) enrichment analysis to identify pathways affected in TAMs at different time points (Fig.1H,I). DEGs are represented by edges (green = up; blue = down) and individual GO terms are represented by nodes. GO terms that are similar, as indicated by the intersection of DEGs in a given GO term, are closer to each other. This generates clusters of similar GO terms indicating common biological processes within the cluster. This analysis revealed a major cluster of upregulated genes related to immunity in TAMs after 5 days (Fig.1H), possibly reflecting a tumoricidal response triggered by resident PM in response to ID8 cells. However, after 21 days, when tumors had become more established, the gene expression profile of TAM more closely resembled the phenotype of naïve PM (Fig.S2). At this later time point, there was an upregulation of distinct gene clusters, including a large cluster of genes related to the innate immune response and tumor necrosis factor (TNF) signaling, in keeping with previous data showing an important role for TNF in this model (Charles et al., 2009), and also a distinctive cluster of genes associated with cholesterol metabolism and efflux (Fig.1I). To confirm the enrichment of genes related to cholesterol homeostasis, we merged several published genesets (Rayner et al., 2011) and known hallmarks to generate an extended gene list representing cholesterol homeostasis. This compiled geneset also showed a significant enrichment in TAMs and among the up-regulated genes were known actors in cholesterol metabolism and efflux, including; *Abcg1*, *Ldlr*, *Pparg*, *Hmgcs1*, *Hmgcr*, *Srebf2* (Fig.S2).

Increased membrane cholesterol efflux in TAMs

Changes in membrane cholesterol content have been shown to dramatically affect macrophage activation in response to pro-inflammatory stimuli, such as bacterial lipopolysaccharide (LPS) (Fessler and Parks, 2011). This is thought, at least in part, to be due to the depletion of cholesterol rich membrane micro-domains, also called lipid rafts, which act as signaling platforms for certain receptors. But membrane cholesterol influences multiple facets of membrane structure and dynamics that can also affect receptor signaling. To confirm the finding that cholesterol efflux pathways were upregulated in TAMs, we sought to measure effects on cholesterol membrane content in TAMs from ID8 tumor bearing mice. Cholesterol rich membrane micro-domains are commonly measured using cholera toxin B (CTB) staining, which binds to ganglioside GM1, the accumulation of which is linked with membrane

cholesterol content. We isolated naïve PM and TAMs at 5 and 21 days after injection of ID8 cells, stained the cells with Alexa Fluor 488-conjugated CTB and analyzed them by confocal microscopy. We observed that CTB staining was similar in naïve PM and TAMs isolated at 5 days, but was significantly decreased in TAMs after 21 days of tumor growth (Fig.2A,B), indicating that the tumor-microenvironment may promote the depletion of cholesterol rich membrane micro-domains in TAMs, in accordance with the upregulation of genes regulating cholesterol efflux in these cells (Fig.1I). To test if ID8 tumor cells had a direct effect on macrophage cholesterol efflux, we co-cultured ID8 cells with bone marrow-derived macrophages (BMDM) *in vitro*. After just one hour of co-culture, there was a significant decrease of CTB staining in BMDM (Fig.2C,D), indicating tumor cells actively promoted the depletion of membrane cholesterol in macrophages. To test if factors secreted by tumor cells were responsible for this effect, we incubated BMDM with conditioned medium obtained from ID8 cell cultures (ID8-CM). This also resulted in a rapid reduction in CTB staining, that was almost equivalent to the effects of methyl-β-cyclodextrin (MCD), which extracts cholesterol from cell membranes (Ostrom and Liu, 2007) (Fig.2E,F). Although CTB is commonly used to measure cholesterol rich membrane micro-domains, this is a rather indirect measure of membrane cholesterol. Another method to asses membrane cholesterol content exploits the highly ordered structure of cholesterol-rich membrane microdomains by the use of phase-sensitive fluorescent probes such as Laurdan and di-4-ANEPPDHQ (Owen et al., 2011). These molecules adapt their emission wavelength based on local membrane order, which is a direct reflection of cholesterol content, independently of membrane-associated proteins. To confirm our findings, we labelled macrophages with di-4-ANEPPDHQ and found a significant decrease of membrane order in the presence of ID8-CM (Fig.2G,H). These assays confirmed that the reduction in CTB staining observed after ID8-CM treatment, correlated with alterations in membrane order that reflect reduced levels of membrane cholesterol. Furthermore, we measured total cholesterol levels in macrophages cultured in the presence or absence of tumor cell-conditioned medium and observed a significant decrease of total cellular cholesterol (Fig.2I). Finally, to directly measure cholesterol efflux from macrophages, we loaded BMDM with thymidine (^{3}H)-labelled cholesterol and measured its efflux into the culture media after addition of the apolipoprotein A1 (ApoA1). Membrane cholesterol efflux is mediated by the transfer of cholesterol to lipoproteins through ABC transporters (Zhao et al., 2010), in the case of ApoA1 this occurs through the transporter ABCA1. These assays showed that addition of ID8-CM significantly increased cholesterol efflux from macrophages, which was reversed in BMDM from ABCA1-deficient mice (*Abca1*$^{-/-}$), demonstrating that this was due to an increased efflux of membrane cholesterol (Fig.2J).

Tumor cell-derived hyaluronic acid (HA) drives cholesterol efflux in macrophages.

The studies described above showed that ID8 cells increased cholesterol efflux from macrophages. This effect could be recapitulated with conditioned medium but not with fixed cells (Fig.3A), indicating that cholesterol efflux is promoted by a secreted factor. In order to further characterize this factor, we exposed ID8-CM to a series of treatments, including ultra-centrifugation, boiling (95^{o}C for 5 min), repeated freeze/thaw cycles, DNAse and proteinase K, none of which had any impact on the ability of ID8-CM to deplete CTB staining in macrophages (data not shown). However, size fractionation of ID8-CM with cut-offs at 3, 10, 30 or 100 kDa, revealed that this activity was present in a fraction with a molecular weight above 100 kDa (Fig.3B). Several previous studies have shown that the extracellular matrix (ECM) component hyaluronic acid (HA) can be produced by tumor cells and has been linked with increased tumor progression (Chanmee et al., 2016). HA also forms high molecular weight oligomers (>100 kDa) with distinct biological activity (Gomez-Aristizabal et al., 2016). Furthermore, receptors for HA are expressed by TAMs, namely CD44 and Lyve-1 (Turley et al., 2002). To test the hypothesis that HA in ID8-CM contributed to the effects on membrane cholesterol content, we treated ID8-CM with hyaluronidase (HAse) to degrade HA. Indeed, ID8-CM treated with HAse was no longer able to deplete CTB staining in macrophages (Fig.3C). Conversely, when HA of different molecular weights was added to macrophages in normal culture medium, we observed a reductiion of CTB staining with increasing molecular weight (Fig.3D). These experiments suggested that high molecular weight HA produced by ID8 cells promotes membrane cholesterol depletion in macrophages. Given that HA is an important component of ECM in many cancers, including EOC (Kolapalli et al., 2016), this suggests HA could affect the phenotype of TAMs through membrane cholesterol depletion.

Cholesterol efflux promotes IL-4 mediated macrophage reprogramming.

Depletion of membrane cholesterol has been shown to profoundly affect macrophage activation in response to pro-inflammatory stimuli (Fessler and Parks, 2011), which suggests that cholesterol efflux in TAMs could affect their programming by signals in the tumor-microenvironment. In some instances, TAMs have been shown to exhibit a tumor-promoting phenotype that can be driven by Th2 cytokines such as IL-4 or IL-13, and are skewed away from the pro-inflammatory and immunostimulatory activation state, induced by Th1 cytokines such as IFNγ (DeNardo et al., 2009). To test the effects of ID8 cells on macrophage reprogramming, we stimulated BMDM with IL-4 or IFNγ in the presence or absence of ID8-CM and measured IL-4 and IFNγ induced gene expression, respectively. ID8-CM pre-treatment profoundly increased the expression of IL-4 induced genes; *Arg1*, *Retnla*, *Chi3l3* and *Mrc1* (Fig.4A). In contrast, ID8-CM inhibited the IFNγ induced expression of *Nos2* and *Il12b* (Fig.4B),

as well as other IFNγ-regulated genes including *Cxcl9*, *Cxcl10* and *Ciita* (Fig.S3), demonstrating that ID8-CM promoted macrophage programming towards an IL-4 induced pro-tumor phenotype. Similar results were obtained after co-culture of ID8 cells with BMDM or with IL-13 treatment, which also signals through the IL4 receptor alpha chain (IL4RA) (Fig.S3). These effects were restricted to the high molecular weight (>100 kDa) fraction of ID8-CM (Fig.S3) and were not sensitive to freeze/thaw cycles, boiling, ultracentrufugation, DNAse or proteinase K treatment (data not shown).

To evaluate the effects of membrane cholesterol depletion on macrophage reprogramming we used several mechanistically distinct treatments to induce cholesterol efflux, in comparison with ID8-CM; 9-cis-retenoic acid (9cRA) upregulates expression of ABC transporters and thereby induces cholesterol efflux (Ricote et al., 2004), whereas high-density lipoprotein (HDL) and ApoA1 strip cholesterol directly from the cell membrane (Zhao et al., 2010). Treatment of BMDM with 9cRA, HDL or ApoA1 resulted in similar levels of reduction in CTB staining as seen upon ID8-CM treatment (Fig.4C), as well as increased IL-4 induced gene expression, while inhibiting IFNγ induced genes (Fig.4D). In contrast, the addition of exogenous cholesterol to BMDM, reduced the effects of ID8-CM on IL-4 induced *Arg1* and IFNγ induced *Nos2* expression (Fig.S3).

These data suggested that membrane cholesterol depletion promotes IL-4 mediated macrophage activation and abrogates IFNγ signalling. To directly test the role of cholesterol efflux in macrophage reprogramming by ID8-CM, we used BMDM from mice with a combined myeloid deficiency in the ABCA1 and ABCG1 reverse cholesterol efflux transporters (*Abca1/g1*$^{\Delta Lyz2}$). Treatment with ID8-CM or other membrane cholesterol-depleting agents failed to reduce CTB staining in BMDM from *Abca1/g1*$^{\Delta Lyz2}$ mice (Fig.4E), which indeed reversed the increase in IL-4 induced gene expression by ID8-CM and the inhibition of IFNγ induced genes (Fig.4F), indicating that membrane cholesterol efflux through ABCA1 and/or ABCG1 promoted IL-4 mediated macrophage activation in the presence of ID8-CM.

Tumor-induced macrophage reprogramming is STAT6 and PI3K-dependent.

To further characterize the mechanisms behind increased IL-4 induced gene expression in the presence of ID8-CM and how this may relate to cholesterol efflux, we analyzed IL-4 receptor signaling pathways. First, we observed no increase in the expression levels of the IL-4 receptor (IL4RA) on macrophages treated with ID8-CM (data not shown), but immunofluorescent staining illustrated an increased intracellular clustering of the receptor that suggested endosomal accumulation, which previously has been shown to promote downstream signaling (Kurgonaite et al.) (Fig.S4). We therefore measured activation of signaling pathways downstream of the IL-4 receptor. IL-4 induced gene expression is regulated by JAK-mediated

phosphorylation of the STAT6 transcription factor. Treatment of BMDM with ID8-CM increased levels of activated STAT6 (pY-STAT6) in response to IL-4 (Fig.5A,D; Fig.S4) while reducing the accumulation of phosphorylated STAT1 (pY-STAT1), upon IFNγ activation (Fig.5B,E; Fig.S4). As expected, IL-4 induced gene expression in the presence of ID8-CM was abolished in BMDM derived from STAT6 deficient mice (*Stat6*$^{-/-}$) (Fig.S4). IL-4 signaling also activates PI3K, which was recently shown to be an important pathway for the tumor-promoting functions of TAM (Kaneda et al., 2016a; Kaneda et al., 2016b), furthermore, increased PI3K signaling has been shown to promote IL-4 induced gene expression in macrophages (Rauh et al., 2005). To assess PI3K activation we measured phosphorylation of the downstream kinase Akt/PKB. We observed a marked increase in serine 473 phosphorylation of Akt (pS-Akt) in the presence of ID8-CM (Fig.5C,F; Fig.S4), this correlated with increased accumulation of phosphatidylinositol (3,4,5)-triphosphate (PIP_3), the product of PI3K activity, as measured by confocal microscopy (Fig.S4). To determine the contribution of PI3K to IL-4 mediated reprogramming in the presence of ID8-CM, we treated cells with the PI3K inhibitor LY294002. As expected, LY294002 treatment blocked the increase in pS-Akt by ID8-CM (Fig.5G) and also abrogated the increase in IL-4 induced *Arg1* and *Chi3l3* expression (Fig.5H,I; Fig.S4), indicating that PI3K activity was critical for ID8-CM induced reprogramming. To determine the role of cholesterol efflux in STAT6 and PI3K activation, we again treated macrophages with 9cRA and ApoA1 to deplete membrane cholesterol, both treatments resulted in similar increases in the accumulation of pY-STAT6 and pS-Akt (Fig.5J,K). Furthermore, macrophages lacking the ABCA1 and ABCG1 cholesterol efflux transporters failed to increase pY-STAT6 and pS-Akt upon treatement with ID8-CM (Fig.5L,M). In addition, increased pY-STAT6 and pS-Akt accumulation was restricted to the high molecular weight (>100 kDa) fraction of ID8-CM and could be reversed by HAse treatment (Fig.S4), indicating that HA-mediated cholesterol efflux promoted increased STAT6 and Akt activation.

The specific accumulation of pS-Akt in the presence of ID8-CM was intriguing, serine 473 phosphorylation of Akt is mediated by mammalian target for rapamycin complex 2 (mTORC2) (Jacinto et al., 2006), which is activated by PI3K through PIP_3 accumulation (Liu et al., 2015). Interestingly, mTORC2 was also recently shown to promote IL-4 induced macrophage activation in response to metabolic stress (Huang et al., 2016). Thus, we hypothesised that ID8-CM induced PIP_3 accumulation could activate mTORC2-mediated pS-AKT phosphorylation and increase IL-4 induced gene expression. In the absence of any specific mTORC2 inhibitors, to test the role of the mTORC complex we used rapamycin, which blocks mTORC1, and Torin which blocks both mTORC1 and mTORC2. Rapamycin treatment only partially inhibited ID8-CM induced pS-Akt accumulation in macrophages, however, Torin treatment completely inhibited ID8-CM induced pS-Akt phosphorylation in a dose-dependent

manner (Fig.5N,O), suggesting that mTORC2 activity is required for ID8-CM induced pS-Akt accumulation in macrophages.
In summary, IL-4 induced macrophage activation or reprogramming in response to ID8-CM requires PI3K-mTORC2-Akt activity and is driven by STAT6.

IL-4-induced STAT6 and PI3K signaling in TAMs drives tumor progression in EOC.

To test the relevance of these pathways for TAMs and tumor progression *in vivo*, we revisited our characterisation of TAMs in ID8 tumors. Our conclusions from the data presented in figure 1, was that monocyte-derived TAMs gradually replaced resident macrophages during tumor progression and that TAMs showed an enrichment for cholesterol efflux pathways (Fig.1I). However, these analyzes were performed on bulk TAM populations, including resident PM and monocyte-derived TAMs. To refine our analysis and determine the specific gene expression signature of monocyte-derived cells, we isolated F4/80^{lo} CCR2^{+} monocytes (MN), alongside F4/80^{hi} LPM, which were further divided into Tim4^{+} and Tim4^{-} subsets (Fig.S5). Tim4 was previously shown to be a marker for proliferative, self-renewing LPM (Rosas et al., 2014), whereas Tim4^{-} F4/80^{hi} cells represent monocyte-derived LPM, which are CCR2-dependent (Fig.1; Fig.S5). First, we collected these 3 populations from naïve mice and at different time points during tumor progression for microarray analysis. We performed a pairwise comparison between the 3 populations in naïve mice and extracted a specific gene signature for each subset, applying a 1.5 FC threshold and a p-value of 0.05. Using the Minimal method (pairwise[Mean(test)/Mean(ref)]), we identified sets of 553 genes specific for MN, 131 for Tim4^{+} PM and 84 for Tim4^{-} PM (Table S1). Given that CCR2 was the highest DEG between Tim4^{-} and Tim4^{+} populations, this strongly supported the monocytic origin of Tim4^{-} cells, in keeping with our previous analysis (Fig.S5). We then used these gene sets to perform enrichment analysis (GSEA) with DEGs from the equivalent 3 subsets in ID8 tumor-bearing mice. This analysis showed a significant down-regulation of the naïve Tim4^{+} PM gene signature and a strong enrichment of the MN and Tim4^{-} gene signatures in Tim4^{+} TAMs (Fig.6A), supporting our conclusion that the tumor-microenvironment promotes the replacement of resident PM with MN-derived cells that acquire a resident-like phenotype, including expression of Tim4 (Fig.1; Fig.S5). To determine the specific genes associated with this phenotype, we extracted the leading edges (LEs) for this enrichment, that is the genes most strongly associated with the enrichment of the MN gene signature in Tim4^{+} TAMs. We identified 173 LEs that were enriched at all time points in Tim4^{+} TAMs (Fig.6B; Table S2), which we then used for Ingenuity Pathway Analysis (IPA). The most significant pathway associated with these genes was the IL-4 pathway (Fig.6B), suggesting that IL-4 in the tumor-microenvironment could be an important upstream regulator for the development of the monocyte-derived TAM phenotype.

To confirm the role of IL-4 signaling in tumor progression *in vivo*, we treated ID8 tumor-bearing mice with an IL-4 receptor blocking monoclonal antibody (αIL4ra) and monitored tumor progression. Treatment with αIL4ra significantly reduced ID8 tumor growth *in vivo* (Fig.6C), suggesting that IL-4 signaling is an important factor for tumor progression in this model. Furthermore, chimeric mice with hematopoietic deficiency in STAT6 (*Stat6*$^{-/-}$) or PI3K (*Pik3cd*$^{-/-}$), also showed significantly reduced tumor growth (Fig.6D,E), indicating that both signaling pathways in tumor stromal cells are important factors for tumor progression. To evaluate the impact of these pathways on TAM phenotype *in vivo*, we sorted bulk TAMs from *Pik3cd*$^{-/-}$ chimeric mice by flow cytometry and isolated RNA for microarray analysis. Expression of *Arg1*, *Il10*, *Ccl2* and *Stab1*, which have previsouly been shown to upregulated in TAMs, were significantly downregulated in macrophages from *Pik3cd*$^{-/-}$ chimeric mice compared to controls (Fig.S5), suggesting that PI3K activation contributes to the TAM phenotype. To further analyze the impact of PI3K activation on TAMs, we generated a gene set from all DEGs between naïve PM and TAMs from wild-type mice. Subsequent GSEA showed a significant enrichment for genes expressed by naïve PM in *Pik3cd*$^{-/-}$ cells (Fig.6F), confirming that PI3K activity contributes to the promotion of the TAM phenotype. In addition, there was no enrichment of genes associated with the IL-4 dependent TAM phenotype (Fig.6G), described above (Fig.6B; Table S2). These data Indicated that PI3K is an important regulator of this gene set in TAMs. Interestingly, using an established gene set for tumoricidal phenotype (GSE26912), which was enriched in naïve PM compared to TAMs, we also observed an enrichment in *Pik3cd*$^{-/-}$ TAMs compared to wild-type cells, suggesting that these cells retained a more tumoricidal phenotype in the absence of PI3K activation (Fig.S5). Finally, to evaluate the role of cholesterol efflux in TAMs *in vivo*, we established ID8 tumors in mice with a myeloid-specific deletion of both ABCA1 and ABCG1 (*Abca1/g1*$^{\Delta Lyz2}$). ID8 tumor progression was significantly impaired in *Abca1/g1*$^{\Delta Lyz2}$ mice compared to littermate controls (Fig.6H). Furthermore, microarray analysis of TAMs sorted from these mice showed a significant downregulation of genes associated with the IL-4 dependent TAM phenotype and a positive enrichment for tumoricidal genes (Fig.6I; Fig.S5), reflecting the phenotype of PI3K deficient TAMs.

Collectively, these data showed that IL-4 signaling in TAMs plays an important role in tumor progression in this model. Furthermore, the PI3K pathway and increased cholesterol efflux, contribute significantly to the functional polarization of TAMs and tumor progression *in vivo*.

Discussion

Here we have studied TAMs in a mouse model of EOC, that reflects the peritoneal spread of HGSC. During tumor progression we showed that MN-derived TAMs accumulate and gradually replace resident macrophages in the peritoneal cavity. We then analyzed the global changes in gene expression in TAMs over time using microarrays and used pathway analysis to reveal changes in gene expression linked with different pathways and biological functions. At early time points, TAMs displayed a more pro-inflammatory gene signature, which strongly distinguished them from naïve resident PM. However, in established tumors, TAMs acquired a phenotype more closely resembling resident PM, which suggested a dynamic reprogramming of TAM phenotype during tumor progression.

Among the pathways upregulated in TAMs from established tumors compared to naïve PM was a cluster of genes related to cholesterol metabolism and reverse cholesterol efflux. Reverse cholesterol efflux in macrophages is regulated by membrane cholesterol efflux transporters, such as ABCA1 and ABCG1. These transporters regulate the levels of cholesterol in the plasma membrane, which has a profound influence on macrophage responses to extracellular stimuli. For example, ABCA1 deficient macrophages accumulate cholesterol in the membrane and are hyperresponsive to pro-inflammatory stimuli, such as bacterial lipopolysaccharide (LPS) (Fessler and Parks, 2011). This is thought to be due to the increase in cholesterol-rich membrane microdomains, also called lipid rafts, which are required to promote TLR4-signaling. However, previous studies have also shown that ABCA1-deficient macrophages are hyporesponsive to other stimuli, including IL-4 and IL-13 (Pradel et al., 2009). Interestingly, ABCG1 deficiency in macrophages was shown to increase their pro-inflammatory phenotype and reduce growth of subcutaneous tumors in mice fed on a high-fat diet (Sag et al., 2015), suggesting that cholesterol accumulation in TAMs can abrogate their pro-tumor functions.

Here, we showed that ovarian cancer cells actively promoted membrane cholesterol efflux in macrophages, which was associated with increased IL-4 signaling and inhibition of IFNγ-induced gene expression, resulting in transcriptional and functional reprogramming of TAMs. Depletion of membrane cholesterol in macrophages increased PI3K activity and mTORC2-mediated Akt phosphorylation. Both PI3K and mTORC2 have previously been linked with IL-4 mediated macrophage activation in different contexts (Huang et al., 2016; Rauh et al., 2005). Furthermore, PI3K was recently shown to be a critical pathway to maintain the pro-tumor functions of TAMs (Kaneda et al., 2016a; Kaneda et al., 2016b). The exact mechanism by which membrane cholesterol regulates PI3K/mTORC2 activation remains to be elucidated. Perhaps cholesterol-rich membrane microdomains are required to recruit negative regulators of PI3K activity, such as the lipid phosphatase SHIP-1. Previous studies have suggested that

SHIP may reside in detergent-resistant membrane fractions (Galandrini et al., 2002) and SHIP-1 is known to inhibit IL-4 signaling in macrophages (Rauh et al., 2005).

The distinct metabolic environment of tumors has long been suggested to influence the phenotype of tumor-infiltrating immune cells, rendering them hyporesponsive and contributing to immune-suppression. Cancer cells rely heavily on cholesterol, which they can scavenge from the tumor-microenvironement through upregulation of apolipoproteins and their receptors (Guillaumond et al., 2015). This may lead to cholesterol depletion in tumor-stromal cells, and particularly TAM which express high levels of the ABCA1 and ABCG1 efflux transporters. Our *in vitro* studies suggest HA could be an important factor produced by cancer cells that promotes this process. HA is a major component of the extracellular matrix (ECM) in many human cancers, including ovarian cancer, and in many cases the degree of HA accumulation strongly correlates with poor prognosis (Kolapalli et al., 2016). Macrophages express at least two distinct receptors for HA; CD44 and Lyve1. Interestingly, CD44 signaling has previously been associated with PI3K activation in TAMs (Lenart et al., 2017). Co-incidentally, PI3K also upregulates ABCA1 expression in macrophages (Okoro et al., 2016), potentially creating a feed-forward loop for enhanced cholesterol efflux and IL-4 mediated reprogramming.

In summary, we describe an important role for membrane cholesterol efflux in the regulation of macrophage activation state in the tumor-microenvironment. Depletion of membrane cholesterol renders macrophages hyperresponsive to pro-tumor signals, such as IL-4, but refractory to activation by the anti-tumor cytokine IFNγ. We propose that cholesterol efflux pathways may represent novel targets to abrogate the pro-tumor functions of TAM while retaining potentially beneficial anti-tumor effects in response to therapy.

Limitations of this study

Despite functional data demonstrating the contribution of IL-4 signaling to tumor progression in this model, IL-4 was not detectable in ascites from tumor-bearing mice, indicating this cytokine is produced at very low levels and consumed rapidly. This illustrates the significance of enhanced sensitivity of TAMs to local concentrations of IL-4, which is increased by several orders of magnitude due to membrane cholesterol depletion. These studies are likely to be relevant to human ovarian cancer, where IL-4 expression has been associated with poor clinical outcome (Candido et al.). The source of IL-4 in this context remains unknown. While other cancer cells, including prostate, breast and bladder, have been shown to express IL-4 (Conticello et al., 2004), conditioned medium from ID8 cells alone was not sufficient to activate IL-4 signaling in macrophages. Other potential sources of IL-4 include $CD4^+$ T cells (DeNardo

et al., 2009), eosinophils (Kratochvill et al., 2015), innate lymphocytes or macrophages themselves.

The precise mechanism by which the activity of ABC transporters is upregulated in TAMs also remains to be elucidated. Cholesterol efflux was rapidly induced upon exposure to tumor-cell conditioned medium and no increase in Abca1 or Abcg1 mRNA was observed (data not shown), suggesting a post-transcriptional mechanism. However, cholesterol efflux was dependent on PI3K activation, associated with increased Akt serine 473 phosphorylation. Other studies have shown serine 473 phosphorylation of Akt regulates the translocation of ABC transporters to the plasma membrane (Huang et al., 2013). This may offer a mechanistic explanation for increased ABC activity in TAMs.

Acknowledgements

We thank Bernard Malissen (CIML, FR) for *Stat6*$^{-/-}$ mice. These studies were supported by grants to TL from: L'Agence Nationale de la Recherche (ANR); ANR-09-MIEN-029-01, ANR-10-BLAN-1302-01 and European Research Council; FP7/2007–2013 Grant agreement number 260753, and institutional funding from INSERM, CNRS and Aix-Marseille-Université. JRV was funded by Marie Curie actions IEF (No.234823). PG was funded by the French Ligue Nationale contre le Cancer (LNCC). AE was funded by the Novo Nordisk Foundation (NNF14OC0008781). Microscopy facilities are supported by ANR-10-INBS-04-01 France Bio Imaging. JLS is a member of the Excellence Cluster ImmunoSensation. The research leading to these results has received funding from the People Programme (Marie Curie Actions) of the European Union's Seventh Framework Programme FP7/2077-2013 under REA grant agreement no. 317445 to JLS.

Author contributions

PG, JRV, AE and TL designed the experiments. PG, JRV, AE performed the experiments with help from OR, VG, CV, MB, NAA. Bioinformatics analysis was performed by MM, TPVM, MD,

OP, TU and JLS. MVE performed cholesterol efflux assays. MT provided *Pik3cd*$^{+/-}$ mice. PG, JRV, AE and TL wrote the manuscript.

Declaration of Interests

The authors declare no competing interests.

References

Bain, C.C., Hawley, C.A., Garner, H., Scott, C.L., Schridde, A., Steers, N.J., Mack, M., Joshi, A., Guilliams, M., Mowat, A.M., et al. (2016). Long-lived self-renewing bone marrow-derived macrophages displace embryo-derived cells to inhabit adult serous cavities. Nat Commun *7*, ncomms11852.

Candido, E.B., Silva, L.M., Carvalho, A.T., Lamaita, R.M., Filho, R.M., Cota, B.D., and da Silva-Filho, A.L. Immune response evaluation through determination of type 1, type 2, and type 17 patterns in patients with epithelial ovarian cancer. Reprod Sci *20*, 828-837.

Chanmee, T., Ontong, P., and Itano, N. (2016). Hyaluronan: A modulator of the tumor microenvironment. Cancer Lett *375*, 20-30.

Charles, K.A., Kulbe, H., Soper, R., Escorcio-Correia, M., Lawrence, T., Schultheis, A., Chakravarty, P., Thompson, R.G., Kollias, G., Smyth, J.F., et al. (2009). The tumor-promoting actions of TNF-alpha involve TNFR1 and IL-17 in ovarian cancer in mice and humans. J Clin Invest *119*, 3011-3023.

Conticello, C., Pedini, F., Zeuner, A., Patti, M., Zerilli, M., Stassi, G., Messina, A., Peschle, C., and De Maria, R. (2004). IL-4 protects tumor cells from anti-CD95 and chemotherapeutic agents via up-regulation of antiapoptotic proteins. J Immunol *172*, 5467-5477.

de Vos van Steenwijk, P.J., Ramwadhdoebe, T.H., Goedemans, R., Doorduijn, E.M., van Ham, J.J., Gorter, A., van Hall, T., Kuijjer, M.L., van Poelgeest, M.I., van der Burg, S.H., et al. (2013). Tumor-infiltrating CD14-positive myeloid cells and CD8-positive T-cells prolong survival in patients with cervical carcinoma. Int J Cancer *133*, 2884-2894.

DeNardo, D.G., Barreto, J.B., Andreu, P., Vasquez, L., Tawfik, D., Kolhatkar, N., and Coussens, L.M. (2009). CD4(+) T cells regulate pulmonary metastasis of mammary carcinomas by enhancing protumor properties of macrophages. Cancer Cell *16*, 91-102.

Fessler, M.B., and Parks, J.S. (2011). Intracellular lipid flux and membrane microdomains as organizing principles in inflammatory cell signaling. J Immunol *187*, 1529-1535.

Galandrini, R., Tassi, I., Mattia, G., Lenti, L., Piccoli, M., Frati, L., and Santoni, A. (2002). SH2-containing inositol phosphatase (SHIP-1) transiently translocates to raft domains and modulates CD16-mediated cytotoxicity in human NK cells. Blood *100*, 4581-4589.

Geissmann, F., Jung, S., and Littman, D.R. (2003). Blood monocytes consist of two principal subsets with distinct migratory properties. Immunity *19*, 71-82.

George, S.H., Garcia, R., and Slomovitz, B.M. (2016). Ovarian Cancer: The Fallopian Tube as the Site of Origin and Opportunities for Prevention. Front Oncol *6*, 108.

Ghosn, E.E., Cassado, A.A., Govoni, G.R., Fukuhara, T., Yang, Y., Monack, D.M., Bortoluci, K.R., Almeida, S.R., Herzenberg, L.A., and Herzenberg, L.A. (2010). Two physically, functionally, and developmentally distinct peritoneal macrophage subsets. Proc Natl Acad Sci U S A *107*, 2568-2573.

Ginhoux, F., and Guilliams, M. (2016). Tissue-Resident Macrophage Ontogeny and Homeostasis. Immunity *44*, 439-449.
Gomez-Aristizabal, A., Kim, K.P., and Viswanathan, S. (2016). A Systematic Study of the Effect of Different Molecular Weights of Hyaluronic Acid on Mesenchymal Stromal Cell-Mediated Immunomodulation. PLoS One *11*, e0147868.
Guillaumond, F., Bidaut, G., Ouaissi, M., Servais, S., Gouirand, V., Olivares, O., Lac, S., Borge, L., Roques, J., Gayet, O., et al. (2015). Cholesterol uptake disruption, in association with chemotherapy, is a promising combined metabolic therapy for pancreatic adenocarcinoma. Proc Natl Acad Sci U S A *112*, 2473-2478.
Hagemann, T., Lawrence, T., McNeish, I., Charles, K.A., Kulbe, H., Thompson, R.G., Robinson, S.C., and Balkwill, F.R. (2008). "Re-educating" tumor-associated macrophages by targeting NF-kappaB. J Exp Med *205*, 1261-1268.
Huang, C.X., Zhang, Y.L., Wang, J.F., Jiang, J.Y., and Bao, J.L. (2013). MCP-1 impacts RCT by repressing ABCA1, ABCG1, and SR-BI through PI3K/Akt posttranslational regulation in HepG2 cells. J Lipid Res *54*, 1231-1240.
Huang, S.C., Smith, A.M., Everts, B., Colonna, M., Pearce, E.L., Schilling, J.D., and Pearce, E.J. (2016). Metabolic Reprogramming Mediated by the mTORC2-IRF4 Signaling Axis Is Essential for Macrophage Alternative Activation. Immunity *45*, 817-830.
Jacinto, E., Facchinetti, V., Liu, D., Soto, N., Wei, S., Jung, S.Y., Huang, Q., Qin, J., and Su, B. (2006). SIN1/MIP1 maintains rictor-mTOR complex integrity and regulates Akt phosphorylation and substrate specificity. Cell *127*, 125-137.
Kaneda, M.M., Cappello, P., Nguyen, A.V., Ralainirina, N., Hardamon, C.R., Foubert, P., Schmid, M.C., Sun, P., Mose, E., Bouvet, M., et al. (2016a). Macrophage PI3Kgamma Drives Pancreatic Ductal Adenocarcinoma Progression. Cancer Discov *6*, 870-885.
Kaneda, M.M., Messer, K.S., Ralainirina, N., Li, H., Leem, C.J., Gorjestani, S., Woo, G., Nguyen, A.V., Figueiredo, C.C., Foubert, P., et al. (2016b). PI3Kgamma is a molecular switch that controls immune suppression. Nature *539*, 437-442.
Kolapalli, S.P., Nunna, V., Thomas, A., Mortha, K.K., Banerjee, S.D., and Boregowda, R.K. (2016). Detection of a specific pattern of hyaluronan oligosaccharides and their binding proteins in human ovarian tumour. Cell Biochem Funct *34*, 217-225.
Kratochvill, F., Neale, G., Haverkamp, J.M., Van de Velde, L.A., Smith, A.M., Kawauchi, D., McEvoy, J., Roussel, M.F., Dyer, M.A., Qualls, J.E., et al. (2015). TNF Counterbalances the Emergence of M2 Tumor Macrophages. Cell Rep *12*, 1902-1914.
Kurgonaite, K., Gandhi, H., Kurth, T., Pautot, S., Schwille, P., Weidemann, T., and Bokel, C. Essential role of endocytosis for interleukin-4-receptor-mediated JAK/STAT signalling. J Cell Sci *128*, 3781-3795.
Lavin, Y., Winter, D., Blecher-Gonen, R., David, E., Keren-Shaul, H., Merad, M., Jung, S., and Amit, I. (2014). Tissue-resident macrophage enhancer landscapes are shaped by the local microenvironment. Cell *159*, 1312-1326.
Lenart, M., Rutkowska-Zapala, M., Baj-Krzyworzeka, M., Szatanek, R., Weglarczyk, K., Smallie, T., Ziegler-Heitbrock, L., Zembala, M., and Siedlar, M. (2017). Hyaluronan carried by tumor-derived microvesicles induces IL-10 production in classical (CD14(++)CD16(-)) monocytes via PI3K/Akt/mTOR-dependent signalling pathway. Immunobiology *222*, 1-10.
Liu, P., Gan, W., Chin, Y.R., Ogura, K., Guo, J., Zhang, J., Wang, B., Blenis, J., Cantley, L.C., Toker, A., et al. (2015). PtdIns(3,4,5)P3-Dependent Activation of the mTORC2 Kinase Complex. Cancer Discov *5*, 1194-1209.
Maere, S., Heymans, K., and Kuiper, M. (2005). BiNGO: a Cytoscape plugin to assess overrepresentation of gene ontology categories in biological networks. Bioinformatics *21*, 3448-3449.
Mantovani, A., Allavena, P., Sica, A., and Balkwill, F. (2008). Cancer-related inflammation. Nature *454*, 436-444.
Merico, D., Isserlin, R., Stueker, O., Emili, A., and Bader, G.D. (2010). Enrichment map: a network-based method for gene-set enrichment visualization and interpretation. PLoS One *5*, e13984.

Noy, R., and Pollard, J.W. (2014). Tumor-associated macrophages: from mechanisms to therapy. Immunity *41*, 49-61.
Oesper, L., Merico, D., Isserlin, R., and Bader, G.D. (2011). WordCloud: a Cytoscape plugin to create a visual semantic summary of networks. Source Code Biol Med *6*, 7.
Okoro, E.U., Guo, Z., and Yang, H. (2016). Akt isoform-dependent regulation of ATP-Binding cassette A1 expression by apolipoprotein E. Biochem Biophys Res Commun *477*, 123-128.
Ostrom, R.S., and Liu, X. (2007). Detergent and detergent-free methods to define lipid rafts and caveolae. Methods Mol Biol *400*, 459-468.
Owen, D.M., Rentero, C., Magenau, A., Abu-Siniyeh, A., and Gaus, K. (2011). Quantitative imaging of membrane lipid order in cells and organisms. Nat Protoc *7*, 24-35.
Pollard, J.W. (2009). Trophic macrophages in development and disease. Nat Rev Immunol *9*, 259-270.
Pradel, L.C., Mitchell, A.J., Zarubica, A., Dufort, L., Chasson, L., Naquet, P., Broccardo, C., and Chimini, G. (2009). ATP-binding cassette transporter hallmarks tissue macrophages and modulates cytokine-triggered polarization programs. Eur J Immunol *39*, 2270-2280.
Rauh, M.J., Ho, V., Pereira, C., Sham, A., Sly, L.M., Lam, V., Huxham, L., Minchinton, A.I., Mui, A., and Krystal, G. (2005). SHIP represses the generation of alternatively activated macrophages. Immunity *23*, 361-374.
Rayner, K.J., Sheedy, F.J., Esau, C.C., Hussain, F.N., Temel, R.E., Parathath, S., van Gils, J.M., Rayner, A.J., Chang, A.N., Suarez, Y., et al. (2011). Antagonism of miR-33 in mice promotes reverse cholesterol transport and regression of atherosclerosis. J Clin Invest *121*, 2921-2931.
Ricote, M., Valledor, A.F., and Glass, C.K. (2004). Decoding transcriptional programs regulated by PPARs and LXRs in the macrophage: effects on lipid homeostasis, inflammation, and atherosclerosis. Arterioscler Thromb Vasc Biol *24*, 230-239.
Rosas, M., Davies, L.C., Giles, P.J., Liao, C.T., Kharfan, B., Stone, T.C., O'Donnell, V.B., Fraser, D.J., Jones, S.A., and Taylor, P.R. (2014). The transcription factor Gata6 links tissue macrophage phenotype and proliferative renewal. Science *344*, 645-648.
Sag, D., Cekic, C., Wu, R., Linden, J., and Hedrick, C.C. (2015). The cholesterol transporter ABCG1 links cholesterol homeostasis and tumour immunity. Nat Commun *6*, 6354.
Schindelin, J., Arganda-Carreras, I., Frise, E., Kaynig, V., Longair, M., Pietzsch, T., Preibisch, S., Rueden, C., Saalfeld, S., Schmid, B., et al. (2012). Fiji: an open-source platform for biological-image analysis. Nat Methods *9*, 676-682.
Schulz, C., Gomez Perdiguero, E., Chorro, L., Szabo-Rogers, H., Cagnard, N., Kierdorf, K., Prinz, M., Wu, B., Jacobsen, S.E., Pollard, J.W., et al. (2012). A lineage of myeloid cells independent of Myb and hematopoietic stem cells. Science *336*, 86-90.
Scott, C.L., Zheng, F., De Baetselier, P., Martens, L., Saeys, Y., De Prijck, S., Lippens, S., Abels, C., Schoonooghe, S., Raes, G., et al. (2016). Bone marrow-derived monocytes give rise to self-renewing and fully differentiated Kupffer cells. Nat Commun *7*, 10321.
Spinelli, L., Carpentier, S., Montanana Sanchis, F., Dalod, M., and Vu Manh, T.P. (2015). BubbleGUM: automatic extraction of phenotype molecular signatures and comprehensive visualization of multiple Gene Set Enrichment Analyses. BMC Genomics *16*, 814.
Subramanian, A., Tamayo, P., Mootha, V.K., Mukherjee, S., Ebert, B.L., Gillette, M.A., Paulovich, A., Pomeroy, S.L., Golub, T.R., Lander, E.S., et al. (2005). Gene set enrichment analysis: a knowledge-based approach for interpreting genome-wide expression profiles. Proc Natl Acad Sci U S A *102*, 15545-15550.
Theocharidis, A., van Dongen, S., Enright, A.J., and Freeman, T.C. (2009). Network visualization and analysis of gene expression data using BioLayout Express(3D). Nat Protoc *4*, 1535-1550.
Turley, E.A., Noble, P.W., and Bourguignon, L.Y. (2002). Signaling properties of hyaluronan receptors. J Biol Chem *277*, 4589-4592.
Urzua, U., Ampuero, S., Roby, K.F., Owens, G.A., and Munroe, D.J. (2016). Dysregulation of mitotic machinery genes precedes genome instability during spontaneous pre-malignant transformation of mouse ovarian surface epithelial cells. BMC Genomics *17*, 728.

Yona, S., Kim, K.W., Wolf, Y., Mildner, A., Varol, D., Breker, M., Strauss-Ayali, D., Viukov, S., Guilliams, M., Misharin, A., et al. (2013). Fate Mapping Reveals Origins and Dynamics of Monocytes and Tissue Macrophages under Homeostasis. Immunity *38*, 79-91.
Zhao, Y., Van Berkel, T.J., and Van Eck, M. (2010). Relative roles of various efflux pathways in net cholesterol efflux from macrophage foam cells in atherosclerotic lesions. Curr Opin Lipidol *21*, 441-453.
Zhu, Y., Herndon, J.M., Sojka, D.K., Kim, K.W., Knolhoff, B.L., Zuo, C., Cullinan, D.R., Luo, J., Bearden, A.R., Lavine, K.J., et al. (2017). Tissue-Resident Macrophages in Pancreatic Ductal Adenocarcinoma Originate from Embryonic Hematopoiesis and Promote Tumor Progression. Immunity *47*, 323-338 e326.

Figure Legends

Figure 1. Ontogeny and phenotype of TAMs during ID8 tumor development.

(**A**) Analysis of PM by flow cytometry after intra-peritoneal (i.p.) injection of 10^6 ID8-Luc cells. PM were gated as; live, single cells (FSC-H versus FSC-W), CD45.2$^+$, Lin$^-$ (NK1.1 Ly6G CD5 CD19), CD11b$^+$, CD64$^+$. LPM were subsequently gated as F4/80^{hi} MHCII$^-$ (blue), intPM as F4/80^{int} MHCII^{int} (orange) and SPM as F4/80$^-$ MHCII^{hi} (green). (**B**) Total numbers of LPM, intPM and SPM during tumor growth. (**C**) Shielded chimeras reconstituted with mixed bone marrow to analyze ontogeny of PM after engraftment with ID8-Luc cells. Host mice (CD45.1) were placed in protective lead shield with only the hind legs exposed, before irradiation with 9 Gy. The following day, mice were reconstituted with a mixture of bone marrow cells from *Ccr2*$^{-/-}$ (CD45.2) and CD45.1/2 congenic mice, at a ratio of 4:1. 5 weeks after reconstitution, mice were injected with ID8-Luc cells. A further 8 weeks after tumor inoculation, PM were collected for analysis. (**D**) Analysis of PM from chimeric mice by flow cytometry; CD45.1 and CD45.2 expression was analyzed on LPM (blue), intPM (orange) and SPM (green), as described above. (**E**) Proportion of chimerism was calculated relative to blood monocytes. (**F**,**G**) Fate mapping of Cx3cr1-expressing monocytes in ID8 tumor-bearing mice; Cx3cr1^{CreER}:R26-tdRFP mice were inoculated with ID8-Luc cells, after 8 weeks 1 mg tamoxifen was administered by oral gavage and RFP expression was analyzed in PM subsets 10 days later. RFP expression within LPM, intPM and SPM is shown. (**H**,**I**) PM were collected from naïve mice and at 5 or 21 days after tumor inoculation by flow cytometry. Total cellular mRNA was extracted and global gene expression profiles analyzed using microarrays. Gene ontology enrichment was perfomed on the differentially expressed genes (DEGs) between naïve PM and TAMs at (**H**) 5 and (**I**) 21 days, respectively. Graphs are represented as mean ± SEM. See also Figures S1 and S2.

Figure 2. Increased membrane cholesterol efflux in TAMs.

(**A**,**B**) PM were isolated from naïve mice (Ctrl) or at 5 and 21 days after inoculation with ID8 cells. Cells were seeded in chambered plastic slides and stained with Cholera Toxin B (CTB; green) and TO-PRO-3 (blue). (**A**) Representative images for all three groups are shown, (**B**) quantification of corrected total cell fluorescence (CTCF). (**C**,**D**) BMDM were co-cultured with ID8 cells for the indicated time points prior to CTB staining, (**C**) representative images for BMDM alone (Ctrl) and 3 hours after ID8 co-culture and (**D**) quantification of CTCF. (**E**-**H**) BMDM were incubated with ID8-CM overnight, or Methyl-β-cyclodextrin for 30 min, prior to CTB staining or di-4-ANEPPDHQ staining; (**E**) representative images for CTB staining in each condition and (**F**) quantification of CTCF. (**G**) Representative images of di-4-ANEPPDHQ staining and (**H**) quantification of relative changes in GP values (Owen et al., 2011). (**I**) Total cell cholesterol content was measured in BMDM with and without ID8-CM treatment, using the Amplex Red Cholesterol Assay kit. (**J**) BMDM from wild-type (WT) or *Abca1*$^{-/-}$ mice were loaded with ^{3}H-labeled cholesterol and subsequently treated or not with ID8-CM in the presence of ApoA1, as an acceptor for cholesterol. ^{3}H-Cholesterol was measured in the medium as a readout for cholesterol efflux. Graphs are represented as mean ± SEM.

Figure 3. Tumor cell-derived hyaluronic acid (HA) oligomers deplete lipid rafts in macrophages.

(**A**) BMDM were co-cultured with live or paraformaldehyde-treated (fixed) ID8 cells, prior to CTB staining, quantification of CTCF is shown. (**B**) High and low molecular weight fractions of ID8-CM were prepared using Centricon filters with 100 kDa pores, each fraction was compared with unfractionated ID8-CM for effects on CTB staining. (**C**) BMDM were treated with ID8-CM with and without hyaluronidase (HAse) treatement prior to CTB staining and quantification. (**D**) BMDM were incubated with HA oligomers of increasing molecular weights before CTB staining and quantification, ID8-CM was used as a positive control. Graphs are represented as mean ± SEM.

Figure 4. Cholesterol efflux promotes IL-4 mediated macrophage reprogramming.

(**A**,**B**) BMDM were treated with or without ID8-CM before stimulation with increasing concentrations of IL-4 or IFNγ for 8 hours. (**A**) Quantitative PCR (qPCR) analysis of IL-4 induced gene expression; *Arg1*, *Chi3l3*, *Mrc1*, *Retnla* and (**B**) IFNγ-induced expression of *Nos2* and *Il12b*. (**C**) BMDM were treated with different cholesterol depleting agents; 9-cis-retenoic acid (9cRA), high-density lipoprotein (HDL) or apolipoprotein A1 (ApoA1), as well as ID8-CM; lipid raft density was subsequently measured by CTB staining, quantification of CTCF is shown. (**D**) IL-4 (20 ng/ml) induced *Arg1* and IFNγ (20 ng/ml) induced *Nos2* expression in

BMDM treated with 9cRA, HDL or ApoA1, compared to ID8-CM. (**E**) BMDM from *Abca1/g1*$^{f/f}$ and *Abca1/g1*$^{\Delta Lyz2}$ mice were incubated with ID8-CM, 9cRA, HDL or ApoA1 and lipid raft density was measure by CTB staining, quantification of CTCF is shown. (**F**) IL-4 induced *Arg1* and IFNγ induced *Nos2* expression in BMDM from *Abca1/g1*$^{f/f}$ and *Abca1/g1*$^{\Delta Lyz2}$ mice with and without ID8-CM treatment. Graphs are represented as mean ± SEM. See also Figure S3.

Figure 5. Tumor-induced reprogramming is STAT6- and PI3K-dependent.

(**A**-**F**) BMDM were treated with or without ID8-CM overnight before stimulation with either IL-4 or IFNγ for 20 min. Cells were then fixed and stained for p-STAT6, p-STAT1 or p-Akt and analyzed by confocal microscopy; representative micrographs for (**A**) p-STAT6, (**B**) p-STAT1 and (**C**) p-Akt staining are shown (green), nuclei are counterstained with TO-PRO-3 (blue). (**D**-**F**) Quantification of CTCF for (**D**) p-STAT6, (**E**) p-STAT1 and (**F**) p-Akt (NS – non stimulated). (**G**-**I**) BMDM were incubated with or without ID8-CM in the presence or absence of the PI3K inhibitor LY294002 (1.25 μM); (**G**) Quantification of p-Akt staining by confocal microscopy and (**H**-**I**) qPCR analysis of IL-4-induced *Arg1* and *Chi3l3* expression. (**J**-**K**) BMDM were incubated overnight with ID8-CM, 9cRA, HDL or ApoA1 before stimulation with IL-4 for 20 min; quantification of (**J**) p-STAT6 and (**K**) p-Akt by confocal microscopy. (**L**-**M**) BMDM from *Abca1/g1*$^{f/f}$ and *Abca1/g1*$^{\Delta Lyz2}$ mice were treated with ID8-CM before stimulation with IL-4 and quantification of (**L**) p-STAT6 and (**M**) p-Akt by confocal micrscopy. (**N**-**O**) BMDM treated with ID8-CM in the presence or absence of Rapamycin (Rapa) or Torin at the indicated concentrations; (**N**) quantification of p-Akt by confocal micrscopy and (**O**) western blot analysis of Ser473 and Thr308 Akt phosphorylation (pAkt(Ser) and pAkt(Thr), respectively) in Rapamycin (R) and Torin (T) treated BMDM with and without ID8-CM treatment. Graphs are represented as mean ± SEM. See also Figure S4.

Figure 6. IL-4-induced STAT6 and PI3K signaling in TAMs drives tumor progression in vivo.

(**A**) Generation of specific gene signatures for Tim4^{+} and Tim4^{-} F4/80^{hi} PM and F4/80^{lo} CCR2^{+} monocytes (MN) using GeneSign (BubbleGUM), cell-specific signatures were assessed for enrichment using BubbleMap (Spinelli et al., 2015), based on the GSEA algorithm in pairwise comparisons of Tim4^{+} PM from naïve mice or ID8 tumor-bearing mice at different time points. The bubble area is proportional to the absolute value of the normalised enrichment score (NES). The color intensity indicates the false-discovery rate (FDR), modified for multiple testing. The size and intensity of color increases with the enrichment of the gene signature from the matching cell population; the Tim4^{+} gene signature is enriched in naïve cells (red),

whereas the Tim4^{-} and MN gene signatures are enriched in TAMs (blue). (**B**) Leading edges (LEs) of the MN gene signature enrichment at different time points (highlighted by colored boxes) were extracted and plotted in a Venn diagram. Ingenuity Pathway Analysis (IPA) was performed on the 173 common LEs, showing IL4 as the top upstream regulator. (**C**) ID8-Luc cells were injected i.p. and mice treated with either IL4Rα blocking antibody (anti-IL4Rα) or an isotype control antbody (Iso-ctrl) after 2 weeks; tumor growth was assessed at 4 weeks by *ex vivo* luciferase assay on peritoneal cells. (**D**-**E**) Cohorts of chimeric mice receiving either wild-type (WT), (**D**) *Stat6*$^{-/-}$ or (**E**) *Pik3cd*$^{-/-}$ bone marrow cells were injected with ID8-Luc cells and tumor growth assessed after 6 weeks. (**F**,**G**) TAMs were isolated from *Pik3cd*$^{-/-}$ chimeric mice and WT controls after 6 weeks of tumor growth by flow cytometry. Microarray analysis was performed to assess geneset enrichment using GSEA. (**F**) Positive enrichment of the naïve PM gene signature in *Pik3cd*$^{-/-}$ TAMs compared to WT cells and (**G**) negative enrichment of the IL-4 pathway signature of TAMs (from **B**) in *Pik3cd*$^{-/-}$ cells. ES plots are shown on the left and the 25 most enriched genes on the right. NES, normalised enrichment score; FDR, false discovery rate. (**H**) *Abca1/g1*$^{f/f}$ and *Abca1/g1*$^{\Delta Lyz2}$ mice were injected with ID8-Luc cells and tumor growth assessed after 6 weeks. (**I**) GSEA with TAMs isolated from *Abca1/g1*$^{f/f}$ and *Abca1/g1*$^{\Delta Lyz2}$ mice showing negative enrichment of the TAM-associated IL4 pathway in *Abca1/g1*$^{\Delta Lyz2}$ mice. Graphs are represented as mean ± SEM. See also Figure S5.

STAR Methods

Key Resources Table

REAGENT or RESOURCE	SOURCE	IDENTIFIER
Antibodies		
anti-Nos2 (M-19)	Santa Cruz	sc-650
anti-Arg1 (N-20)	Santa Cruz	sc-18351
HRP-conjugated anti-Rabbit immunoglobulins	DAKO	P044801-2
HRP-conjugated anti-Mouse immunoglobulins	DAKO	P026002-2
anti-β-Actin (AC-74)	Sigma	A5316
anti-Akt (40D4)	Cell Signaling	2920
anti-pSer473-Akt (D9E)	Cell Signaling	4060
anti-pThr308-Akt (D25E6)	Cell Signaling	13038
anti-STAT1	Cell Signaling	9172
anti-pTyr701-STAT1	Cell Signaling	9171
anti-STAT6 (M-20)	Santa Cruz	sc-981
anti-pTyr641-STAT6	Cell Signaling	9361
anti-PIP3	Invitrogen	A-21328
Anti-CD124	Novus Biologicals	NBP1-00884
anti-CD11b (M1/70)	BD Biosciences,	563553

anti-CD45.1 (A20)	BD Biosciences	553775
anti-NK1.1 (PK136)	BioLegend	108724
anti- Ly6G (1A8)	BD Biosciences	560600
anti- CD5 (53-7.3)	BD Biosciences	563194
anti-CD19 (1D3)	BD Biosciences	565076
anti-CD64 (X54-5/7.1	BioLegend	139311
anti-Ly6C (AL-21)	BD Biosciences	553104
anti-MHCII (M5/114)	eBioscience	56-5321-82
anti-F4/80 (BM8)	BioLegend	123141
anti-Lyve-1 (ALY7)	eBioscience	53-0443-82
anti-rabbit-Alexa488	Invitrogen	A-10040
Chemicals, Peptides, and Recombinant Proteins		
LY294002	R&D Systems	1130
Rapamycin	Merck	553211
Hyaluronic acid	Lifecore Biomedical	HA15M-1
Hyaluronidase	Sigma	H3506
Torin	Sigma	475991
Methyl-β-cyclodextrin	Sigma	C4555
High-density lipoprotein	Sigma	L8039
9-cis-retenoic acid	Sigma	R4643
Cholesterol-methyl-β-cyclodextrin	Sigma	C4951
Proteinase inhibitor cocktail	Sigma	P8340
Xylazine	Sigma	23076-35-9
PNPP	Sigma	333338-18-4
β-glycerophosphate	Sigma	G9422
DTT	Sigma	43819
Apolipoprotein A1	Sigma	A0722
Recombinant mouse IL4	Peprotech	214-14
Recombinant mouse IFNγ	Peprotech	315-05
Recombinant mouse M-CSF	Peprotech	315-02
Recombinant mouse IL13	Peprotech	210-13
Vybrant Alexa Fluor 488 Lipid Raft Labelling Kit	ThermoFisher Scientific	V34403
TRIzol	ThermoFisher Scientific	15596018
di-4-ANEPPDHQ	ThermoFisher Scientific	D36802
TO-PRO-3	ThermoFisher Scientific	T3605
SYBR Green PCR Master Mix	ThermoFisher Scientific	4312704
IL4Rα neutralizing antibody	BD Biosciences	552508
Critical Commercial Assays		
Superscript IV Reverse Transcriptase	ThermoFisher Scientific	18090050
Amplex Red Cholesterol Assay kit	ThermoFisher Scientific	A12216
Deposited Data		
GSE126079	This paper	https://www.ncbi.nlm.nih.gov/geo/query/acc.cgi?acc=GSE126079
GSE126080	This paper	https://www.ncbi.nlm.nih.gov/geo/query/acc.cgi?acc=GSE126080
GSE126098	This paper	https://www.ncbi.nlm.nih.gov/geo/query/acc.cgi?acc=GSE126098

GSE126378	This paper	https://www.ncbi.nlm.nih.gov/geo/query/acc.cgi?acc=GSE126378
Experimental Models: Cell Lines		
Bone marrow derived macrophages	This paper	Hagemann et al., 2008
ID8-Luc ovarian surface epithelial cell line	Prof. Frances Balkwill	Barts Cancer Institute, London, UK
Experimental Models: Organisms/Strains		
Mouse: C57Bl/6	Charles River	JAX 000664
Mouse: Abca1^{tm1Jp} Abcg1^{tm1Tall}	Jackson Laboratories	Stock number 021067
Mouse: Lyz2$^{tm1(cre)Ifo}$	Jackson Laboratories	Stock number 004781
Mouse: Stat6$^{-/-}$	Dr. Bernard Malissen	CIML, Marseille, FR
Mouse: Abca1$^{-/-}$	Prof. Miranda van Eck	Leiden University, NL
Mouse: Cx3cr1$^{+/eGFP}$	Jackson Laboratories	Stock number 005582
Cx3cr1$^{cre/ERT2}$	Prof. Steffen Jung	Department of Immunology, The Weizmann Institute of Science, Rehovot, Israel.
Mouse: Pik3cd$^{-/-}$	Prof. Martin Turner	Babraham Institute, Cambridge, UK
Oligonucleotides		
Primers for mRNA expression	This paper	See Table S1
Software and Algorithms		
FIJI software	(Schindelin et al., 2012)	https://fiji.sc/
FACS DiVa software	BD Biosciences	https://www.bdbiosciences.com/
FlowJo cytometric analytical software	Tree Star	https://www.flowjo.com/solutions/flowjo
Gene Set Enrichment Analysis (GSEA)	Broad Institute	(Subramanian et al., 2005)
Affymetrix Expression Console version 1.1 software	Affymetrix	https://www.thermofisher.com/be/en/home/global/forms/life-science/download-tac-software.html
Prism software	Graphpad	www.graphpad.com
BioLayout Express3D		(Theocharidis et al., 2009)

CONTACT FOR REAGENT AND RESOURCE SHARING

Further information and requests for resources and reagents should be directed to and will be fulfilled by Toby Lawrence (toby.lawrence@kcl.ac.uk).

EXPERIMENTAL MODEL DETAILS

Mice

C57Bl/6 mice were obtained from Charles River. All transgenic mouse strains were backcrossed to a C57Bl/6 background. *Abca1*^{tm1Jp} *Abcg1*^{tm1Tall} (*Abca1/g1*$^{f/f}$) and *Lyz2*$^{tm1(cre)Ifo}$ (*Lyz2*^{Cre}) mice were obtained from Jackson Laboratories. *Stat6*$^{-/-}$ mice were kindly donated by Dr. Bernard Malissen (CIML, Marseille, FR), *Abca1*$^{-/-}$ mice by Prof. Miranda van Eck (Leiden University, NL) and *Pik3cd*$^{-/-}$ mice by Prof. Martin Turner (Babraham Institute, Cambridge, UK). Generation of shielded chimeras was performed as previously described (Scott et al., 2016); briefly, CD45.1 congenic mice were anaesthetized with Ketamine (150 mg/kg) and Xylazine (10 mg/kg) and placed in 6 mm thick lead cylinders, exposing only the hind legs. With the peritoneal cavity protected, mice were irradiated with 9 Gy and reconstituted with 10^7 bone marrow cells from *Ccr2*$^{-/-}$ (CD45.2) and CD45.1/2 mice, at a ratio of 4:1. After 5 weeks, chimerism of blood leukocytes was assessed by flow cytometry. All mice were housed under specific pathogen-free conditions at a temperature of 21°C with water and food *ad libitum*, and animal experimentation was conducted in strict accordance with good animal practice as defined by the French animal welfare bodies relative to European Convention (EEC Directive 86/609) and approved by the Direction Départmentale des Services Vétérinaires des Bouches du Rhônes. All the mice used were female, did not have impaired immunity and were aged between 8 and 12 weeks and showed no noticeable signs of sickness or discomfort at the onset of the experiments.

METHOD DETAILS

Cell Culture

Bone marrow derived macrophages (BMDM) were obtained as previously described (Hagemann et al., 2008); briefly, femurs and tibiae from mice aged 8 to 10 weeks were flushed and cells collected by centrifugation at 450 g for 5 min at 4°C. Cells were resuspended in DMEM supplemented with L-glutamine (2 mM), penicillin (100 U/ml)/streptomycin (100 μg/ml) (Gibco), 10 % heat-inactivated FBS and 10 ng/ml recombinant mouse M-CSF (Peprotech) and cultured at a density of 10^6 cells/ml in non-tissue culture treated plastic dishes (BD Pharmingen) at 37°C and 5 % CO_2. After 7 days, adherent cells were collected and resuspended in complete DMEM containing 10 ng/ml M-CSF. The ID8-Luc ovarian surface epithelial cell line was kindly provided by Prof. Frances Balkwill (Barts Cancer Institute, London, UK). To obtain ID8 cell-conditioned conditioned medium (ID8-CM); 13.75 x10^6 cells in 25 ml were incubated for 72 hours in a 175 cm^2 flasks in DMEM containing 4% of FCS. Medium was filtered through a .22 μM filter, aliquoted and stored at -80°C.

Immunofluorescence and lipid raft staining

BMDM were grown in Lab-Tek chambered slides (ThermoFisher Scientific) and fixed with 4 % PFA, permeabilized (0.1 % Triton-X100) and blocked in 5 % BSA with 10 mM glycine. The following primary antibodies were used for incubation during 90 minutes at 4°C; anti-pSTAT1, anti-pSTAT6, anti-pSer473-Akt, anti-pThr308-Akt, anti-PIP_3 (Cell Signaling) or anti-IL4Rα (Novus biologicals). After washing, anti-rabbit-Alexa488 (Invitrogen) and TO-PRO-3 (ThermoFisher Scientific) were added for 60 minutes. Lipid rafts were stained using the Vybrant Alexa Fluor 488 Lipid Raft Labelling Kit (ThermoFisher Scientific), following manufacturer's instructions. Briefly, BMDM were grown and stimulated in Lab-Tek chambered slides. After washing with serum-free DMEM, they were incubated for 10 minutes with Alexa488-conjugated cholera toxin subunit B (CTB) at 4°C, followed by cross-linking with an anti-CTB antibody for 15 minutes at 4°C. Subsequently, the cells were fixed with 4 % Antigenfix (DiaPath) for 10 minutes on ice and nuclei were stained with TO-PRO-3. The di-4-ANEPPDHQ lipid raft staining protocol was adapted from the one described by Owen et al. (Owen et al., 2011). Briefly, culture medium was replaced with fresh, serum-free DMEM containing 2 µl of di-4-ANEPPDHQ (5 µM). Dishes were shaken to ensure good mixing. After 30 min incubation at 37 °C in a humidified 5 % CO_2 atmosphere, cells were fixed with 4 % PFA. Fluorescence was measured by confocal microscopy (Zeiss LSM780 or Leica SP5X) and blindly analyzed with FIJI software. The corrected total cell fluorescence (CTCF) was measured for each cell in at least 6 different fields of view per well.

Cholesterol measurement

Total cell cholesterol content was measured in BMDM using the Amplex Red Cholesterol Assay kit (ThermoFisher Scientific), according to the manufacturer's instructions.

Immunoblotting

BMDM were lysed on ice in lysis buffer supplemented with proteinase inhibitor cocktail, PNPP, β-glycerophosphate and DTT. Separation by SDS-PAGE was followed by blotting on PVDF membrane. Blots were blocked with 5 % skimmed milk in TBS-0.05 %Tween20. The following primary antibodies were used; anti-Nos2, anti-Arg1 (Santa Cruz), anti-β-Actin (Sigma), anti-Akt, anti-pSer473-Akt, anti-pTyr701-STAT1, anti-STAT1, anti-pTyr641-STAT6 (Cell Signaling) and anti-STAT6 (Santa Cruz). Primary antibodies were incubated overnight at 4°C and appropriate HRP-conjugated secondary antibodies (DAKO) for 1 hour at room temperature. Chemoluminescence was detected by Pierce ECL Western Blotting Substrate (Thermo Scientific).

Gene expression analysis

Total cellular RNA was extracted from BMDM using TRIzol and cDNA was synthesised with cDNA Synthesis Kit (Thermo Fisher Sientific) according to the manufacturer's protocol. Gene expression was quantified using sequence specific primers in the presence of SYBR Green PCR Master Mix using an ABI 7900HT thermocycler (Applied Biosystems). Reactions were performed in duplicate or triplicate and Ct-values were normalised to the mean Ct-values of cyclophillin. Relative quantification of gene expression was calculated as 2ΔΔCt to controls. Primers used for RT-qPCRs are shown as part of the Supplementary data.

Ovarian cancer model

One million ID8 cells were injected intraperitoneally in the different mouse strains using a 27G syringe. Mice were euthanized at the indicated times and peritoneal lavages were collected for cytometric analysis, *ex vivo* bioluminescence measurement and/or lipid raft staining. Briefly, 9 ml of ice-cold PBS was injected intraperitoneally and after a careful massage to detach all the cells in the cavity, peritoneal fluid was collected through a 23G syringe. Tubes were weighed to determine the recovered lavage volume and the cell density was assessed using a Casy cell counter (Innovatis). Cells were centrifugated and resuspended in 1 ml cold PBS. One million cells from each peritoneal lavage were stained for flow cytometry. 50 µl of the 1 ml cell suspension obtained from peritoneal lavage was used for luciferase activity measurements. Cells were plated in a white 96-well plate and 50 µl luciferin was added to each well, Luminescence [photons/s] was measured for each well using the Mithras Microplate Reader (Berthold Technologies).

Flow Cytometry

Peritoneal lavage cells underwent a short NH_4Cl red blood cell lysis and were incubated at 4°C for 10 min with the 2.4.G2 antibody to block Fc receptors. The cells were stained with the indicated antibodies for 30 min at 4°C. Dead cells were gated out using SYTOX Blue dead cell stain (Life Technologies). After cell-surface staining, cells were fixed. Analysis was performed using an LSR-II flow cytometer or sorted using an Aria III cell sorter (both BD Biosciences) and data analysis was conducted with the FlowJo cytometric analytical software (Tree Star). Anti-CD11b (M1/70), anti-CD44 (IM7), anti-CD45.1 (A20), anti-CD45.2 (104), NK1.1, Ly6G, anti-CD5 (53-7.3), anti-CD19 (1D3), anti-CD64, anti-Ly6C (AL-21), anti-F4/80 and anti-MHCII (M5/114) were purchased from BD Biosciences, eBioscience, BioLegend, and Life Technologies.

Microarray Analysis

RNA samples were hybridized on Affymetrix Mouse 430 2.0 or MoGene 1.0 st chips. Samples were processed as follows: The biotinylated cRNAs were prepared according to a double amplification protocol using MessageAmp™ II aRNA Amplification Kit (Ambion). The images of the chips were generated with Affymetrix software AGCC version 3.2. The expression data was then extracted with the Affymetrix Expression Console version 1.1 software using the RMA (log2 scale) and MAS5 (linear scale) algorithms. Gene Set Enrichment Analysis (GSEA, Broad Institute) (Subramanian et al., 2005) was used to examine differentially expressed genes (DEGs). The output of GSEA is an enrichment plot (ES), a normalized enrichment score (NES) which accounts for the size of the gene set being tested, a p-value, and an estimated False Discovery rate (FDR). We computed P values using 1,000 permutations for each gene set and corrected them with the false-discovery rate (FDR) method. When several probe sets were present for a gene, the mean of the probe set was used. Cell-specific gene sets were generated by performing pairwise comparisons between DEGs from different populations, applying a 1.5 FC threshold and a p value of 0.05, using the Minimal (pairwise[Mean(test)/Mean(ref)]) method. Sample correlation analysis was performed based on Pearson's correlation coefficients using BioLayout Express3D (Theocharidis et al., 2009). GO enrichment analysis was applied using the Cytoscape plug-in BiNGO (v2.44) (Maere et al., 2005) with FDR q-value threshold of 0.05 as default. The Cytoscape plugins Enrichment Map (v1.1) (Merico et al., 2010) and Word Cloud (Oesper et al., 2011) were used to visualize the GO networks. Accession numbers for datasets are; GSE126079, GSE126080, GSE126098.

QUANTIFICATION AND STATISTICAL ANALYSIS

Graphs were made and statistical analysis was performed using Prism software (Graphpad). All quantitative data are presented as mean ± SEM. The statistical parameters (n, mean, SEM) can be found within the figure legends. The t-test was used to define differences between 2 datasets. To define differences between 3 or 4 datasets, One-way Analysis of Variance (ANOVA) was used with a Bonferroni multiple comparison post-test. The criterion for significance was set at $P<0.05$. No statistical method was used to determine whether the data met assumptions of the statistical approach.

DATA AND SOFTWARE AVAILABILITY

The accession numbers for the microarray data reported in this paper are: GSE126079, GSE126080, GSE126098 and GSE126378.

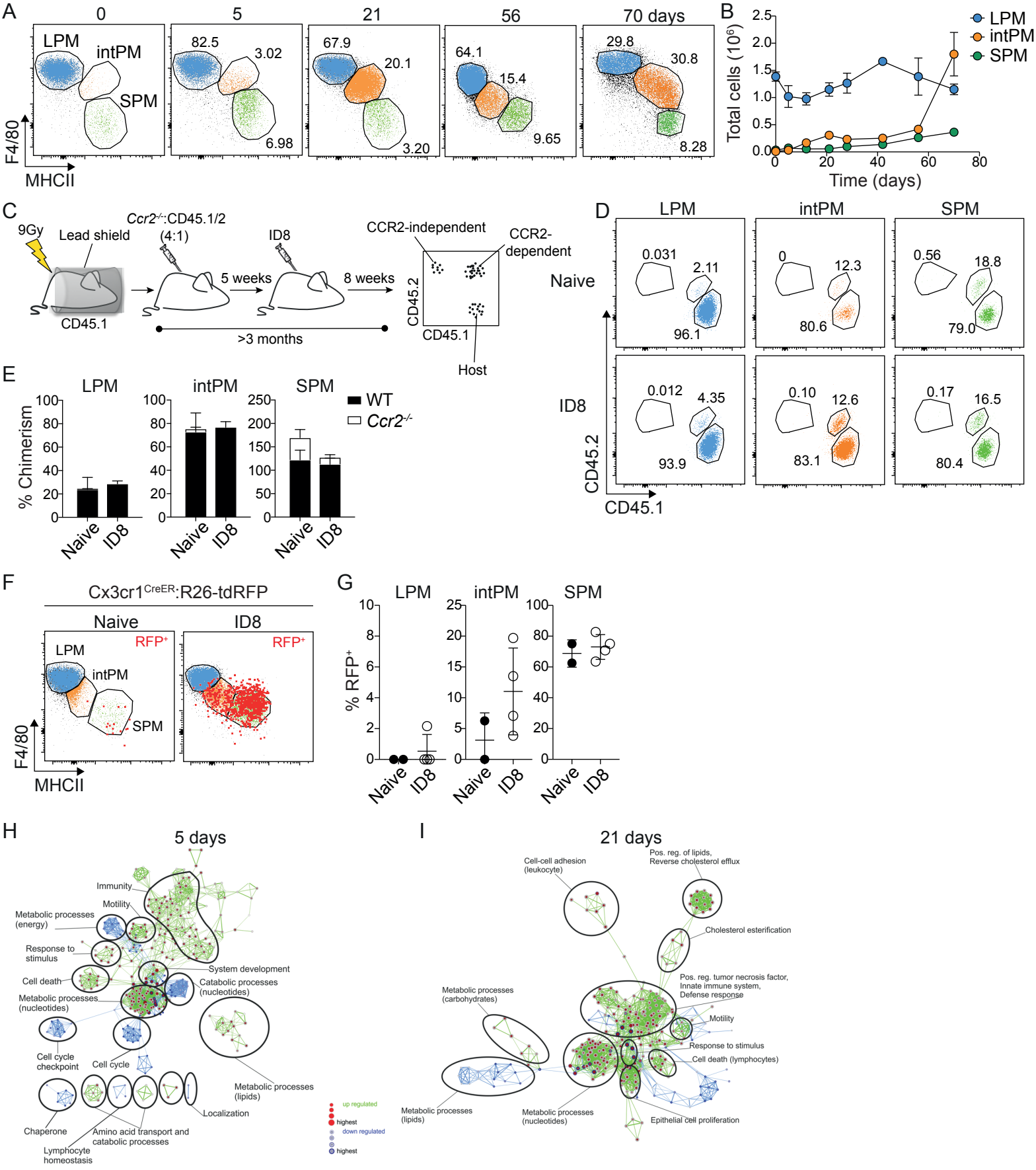
A
0
5
21
56
70 days
LPM
intPM
SPM
82.5
3.02
6.98
67.9
20.1
3.20
64.1
15.4
9.65
29.8
30.8
8.28
F4/80
MHCII
B
Total cells (10^6)
Time (days)
C
9Gy
Lead shield
Ccr2-/-:CD45.1/2
(4:1)
ID8
5 weeks
8 weeks
>3 months
CD45.1
CCR2-independent
CCR2-dependent
CD45.2
Host
D
LPM
intPM
SPM
Naive
ID8
0.031
2.11
96.1
0
12.3
80.6
0.56
18.8
79.0
0.012
4.35
93.9
0.10
12.6
83.1
0.17
16.5
80.4
CD45.2
CD45.1
E
% Chimerism
WT
Ccr2-/-
Naive
ID8
F
Cx3cr1CreER:R26-tdRFP
RFP+
G
% RFP+
H
5 days
Immunity
Motility
Metabolic processes (energy)
Response to stimulus
System development
Cell death
Catabolic processes (nucleotides)
Metabolic processes (nucleotides)
Cell cycle checkpoint
Cell cycle
Metabolic processes (lipids)
Localization
Chaperone
Amino acid transport and catabolic processes
Lymphocyte homeostasis
up regulated
highest
down regulated
I
21 days
Cell-cell adhesion (leukocyte)
Pos. reg. of lipids, Reverse cholesterol efflux
Cholesterol esterification
Pos. reg. tumor necrosis factor, Innate immune system, Defense response
Metabolic processes (carbohydrates)
Motility
Response to stimulus
Cell death (lymphocytes)
Metabolic processes (lipids)
Metabolic processes (nucleotides)
Epithelial cell proliferation

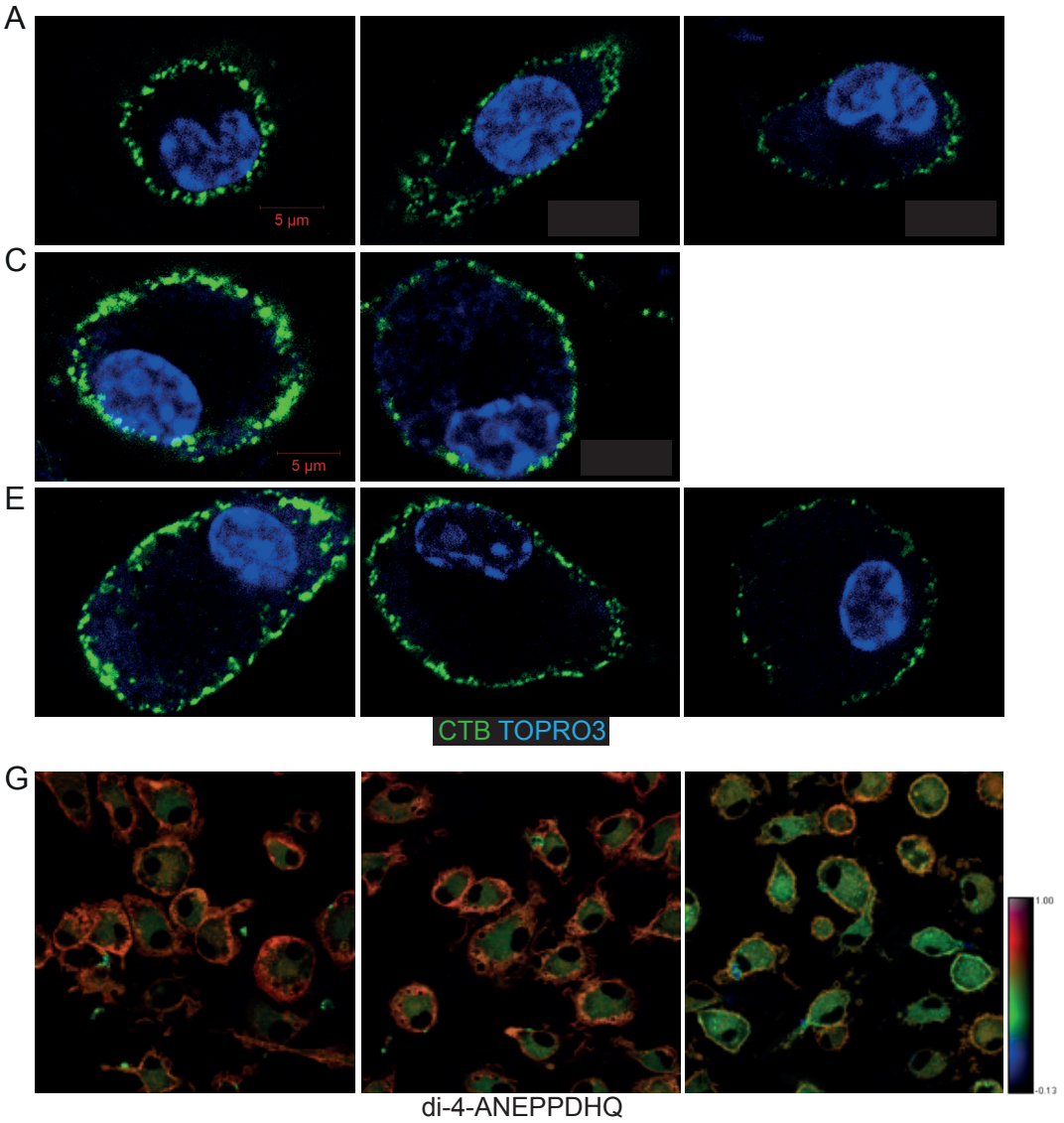
A
5 µm
C
5 µm
E
CTB TOPRO3
G
di-4-ANEPPDHQ

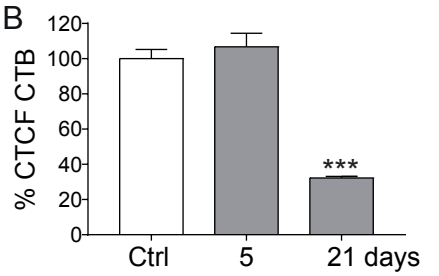
B
% CTCF CTB
120
100
80
60
40
20
0
***
Ctrl
5
21 days

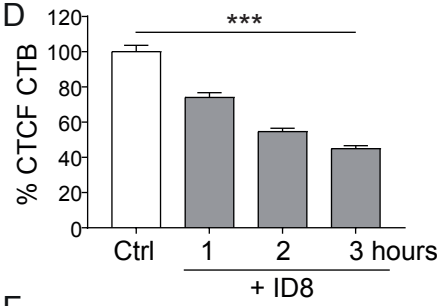
D
% CTCF CTB
120
100
80
60
40
20
0
***
Ctrl
1
2
3 hours
+ ID8

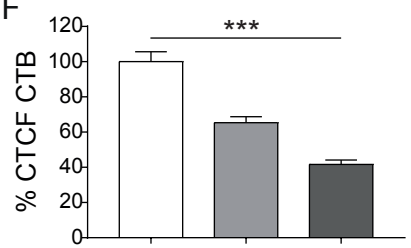
F
% CTCF CTB
120
100
80
60
40
20
0
***
Ctrl
ID8-CM
MCD

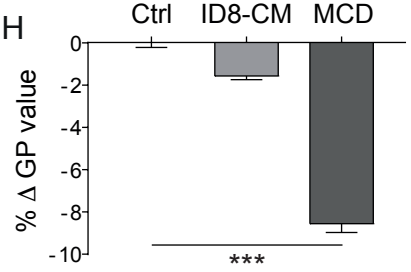
H
% Δ GP value
0
-2
-4
-6
-8
-10
***

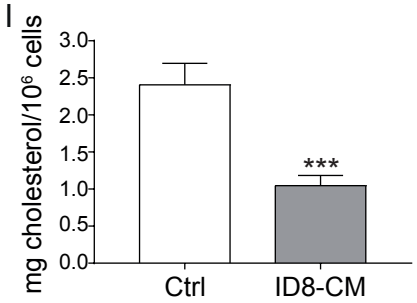
I
mg cholesterol/10⁶ cells
3.0
2.5
2.0
1.5
1.0
0.5
0.0
***
Ctrl
ID8-CM

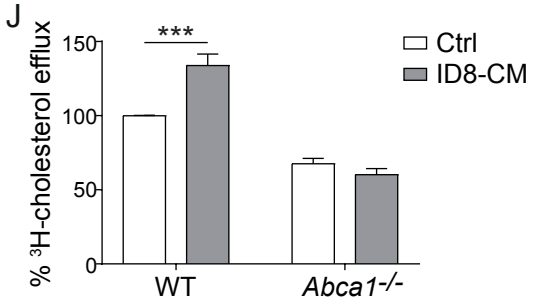
J
% ³H-cholesterol efflux
150
100
50
0
***
Ctrl
ID8-CM
WT
Abca1-/-

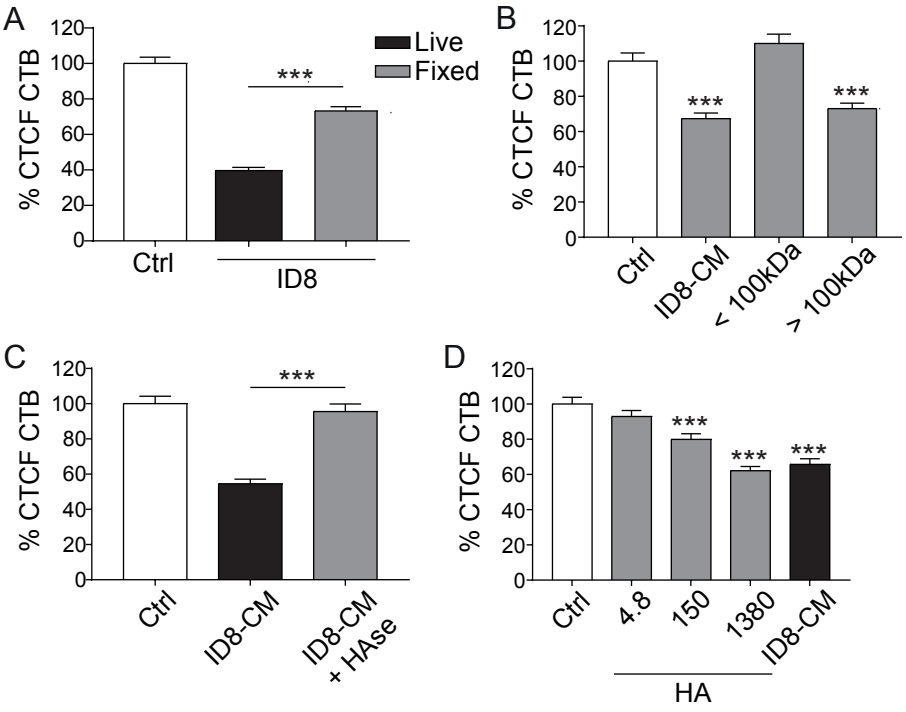
A
% CTCF CTB
120
100
80
60
40
20
0
Live
Fixed
***
Ctrl
ID8
B
% CTCF CTB
***
***
Ctrl
ID8-CM
< 100kDa
> 100kDa
C
% CTCF CTB
***
Ctrl
ID8-CM
ID8-CM + HAse
D
% CTCF CTB
***
***
***
Ctrl
4.8
150
1380
ID8-CM
HA

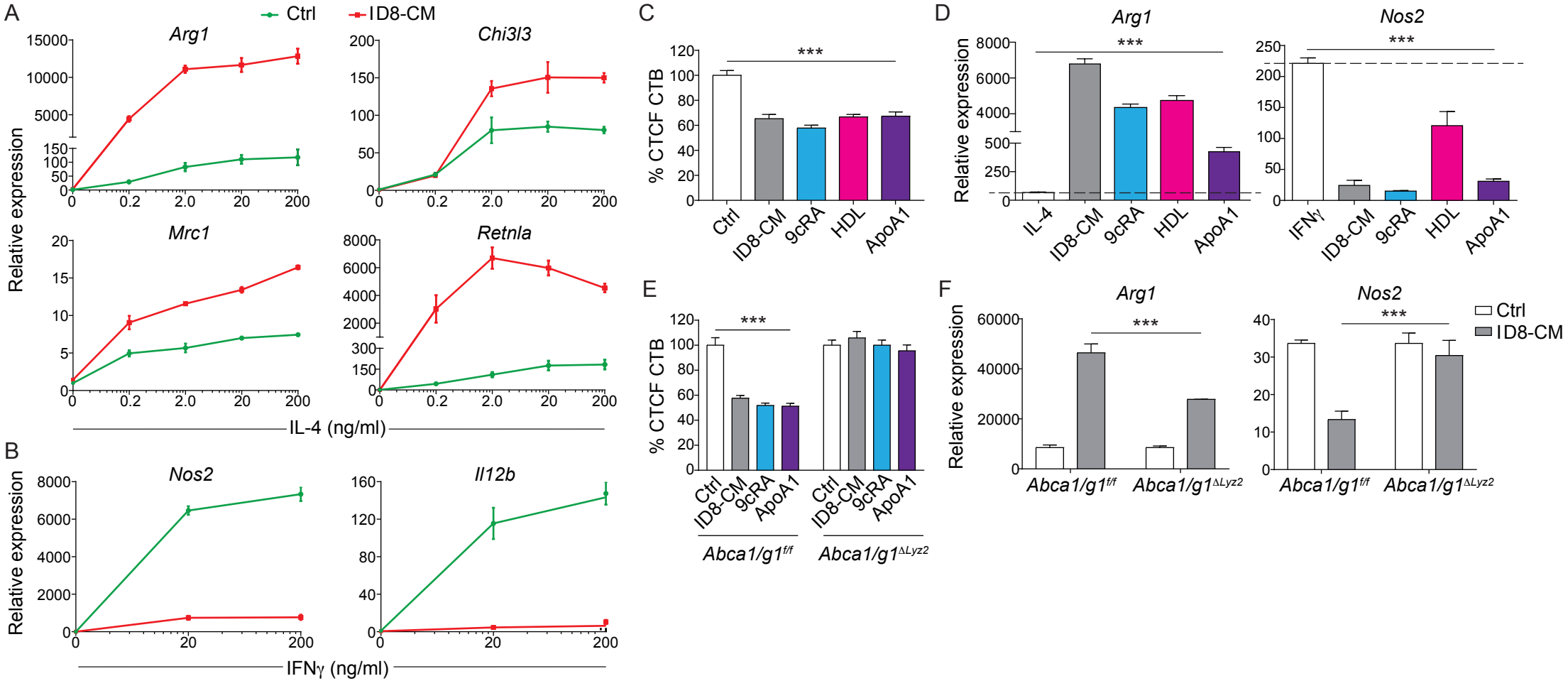
A
Ctrl
ID8-CM
Arg1
Chi3l3
Mrc1
Retnla
Relative expression
IL-4 (ng/ml)
B
Nos2
Il12b
Relative expression
IFNγ (ng/ml)
C
% CTCF CTB
***
Ctrl
ID8-CM
9cRA
HDL
ApoA1
D
Arg1
Nos2
Relative expression
***
IL-4
IFNγ
E
% CTCF CTB
***
Abca1/g1f/f
Abca1/g1ΔLyz2
F
Arg1
Nos2
Relative expression
***
Ctrl
ID8-CM
Abca1/g1f/f
Abca1/g1ΔLyz2

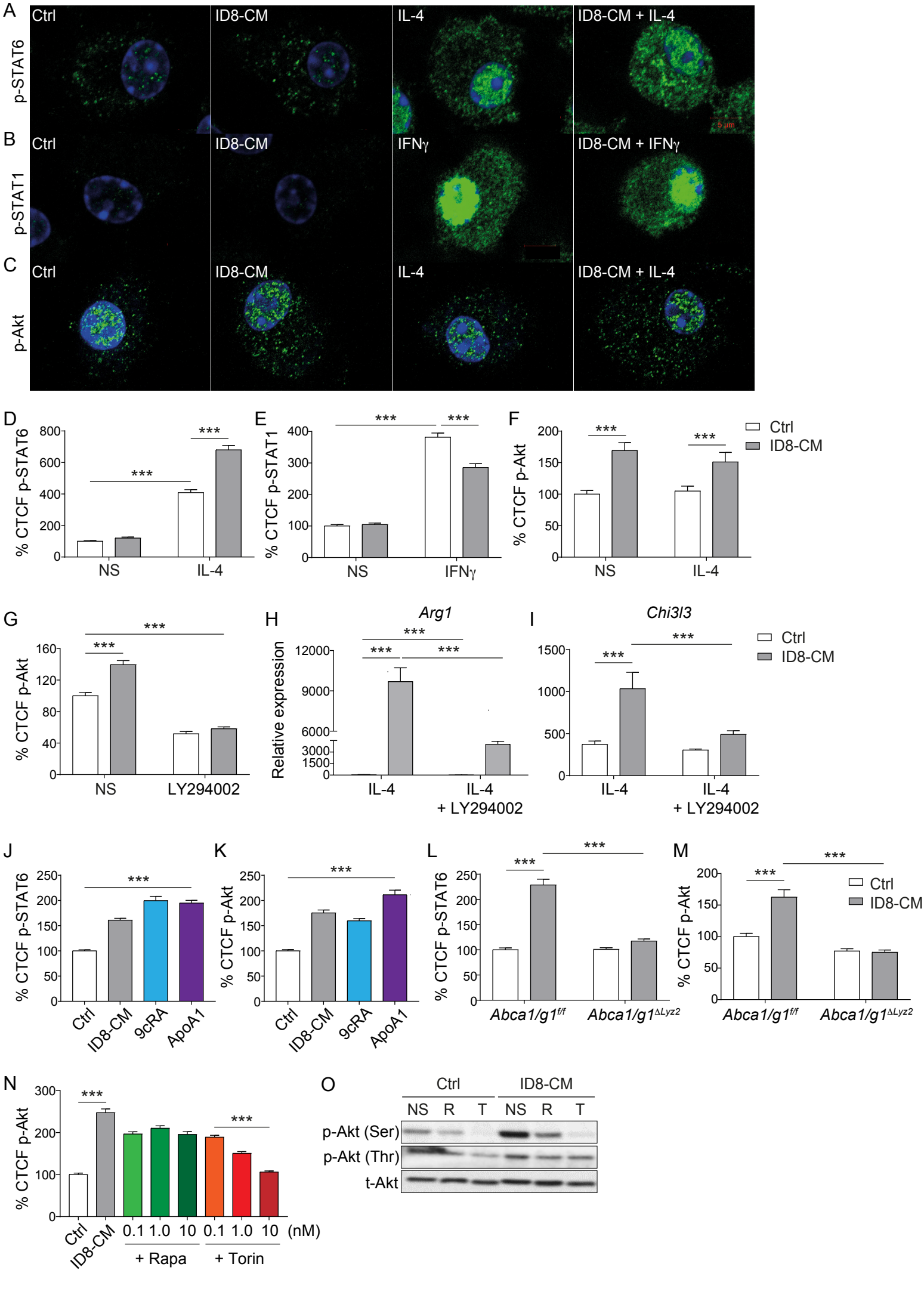
A
p-STAT6
Ctrl
ID8-CM
IL-4
ID8-CM + IL-4
B
p-STAT1
Ctrl
ID8-CM
IFNγ
ID8-CM + IFNγ
C
p-Akt
Ctrl
ID8-CM
IL-4
ID8-CM + IL-4
D
% CTCF p-STAT6
NS
IL-4
E
% CTCF p-STAT1
NS
IFNγ
F
% CTCF p-Akt
NS
IL-4
Ctrl
ID8-CM
G
% CTCF p-Akt
NS
LY294002
H
Arg1
Relative expression
IL-4
IL-4 + LY294002
I
Chi3l3
IL-4
IL-4 + LY294002
Ctrl
ID8-CM
J
% CTCF p-STAT6
Ctrl
ID8-CM
9cRA
ApoA1
K
% CTCF p-Akt
Ctrl
ID8-CM
9cRA
ApoA1
L
% CTCF p-STAT6
Abca1/g1f/f
Abca1/g1ΔLyz2
M
% CTCF p-Akt
Abca1/g1f/f
Abca1/g1ΔLyz2
Ctrl
ID8-CM
N
% CTCF p-Akt
Ctrl
ID8-CM
0.1 1.0 10 0.1 1.0 10 (nM)
+ Rapa
+ Torin
O
Ctrl
ID8-CM
NS R T NS R T
p-Akt (Ser)
p-Akt (Thr)
t-Akt

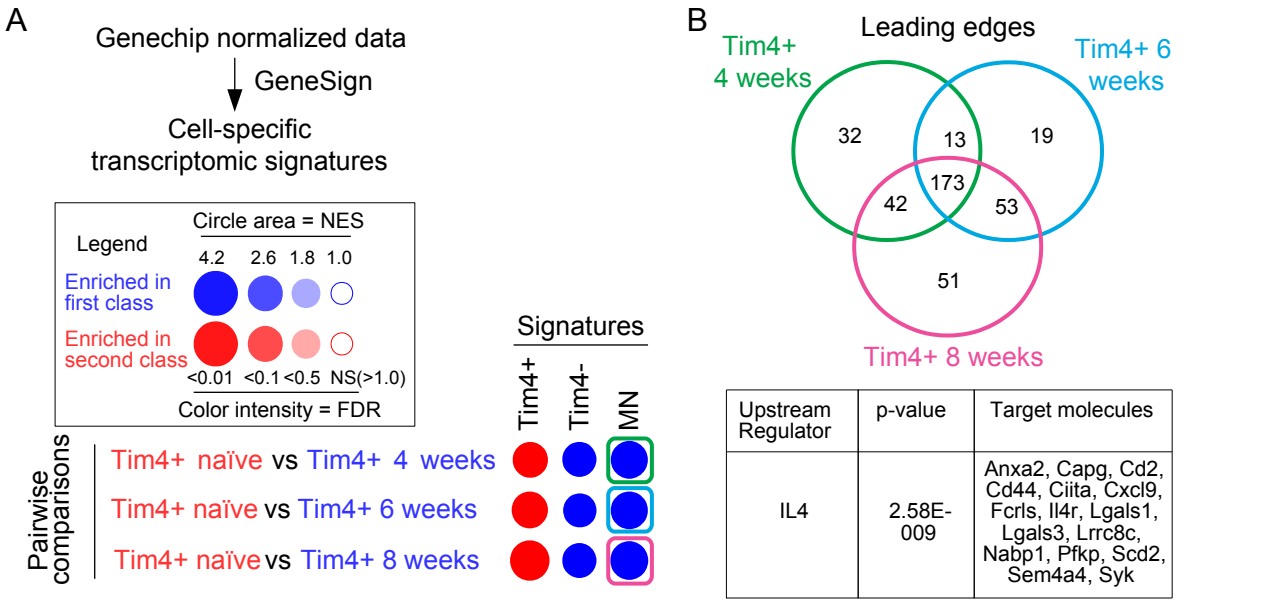

Upstream Regulator	p-value	Target molecules
IL4	2.58E-009	Anxa2, Capg, Cd2, Cd44, Ciita, Cxcl9, Fcrls, Il4r, Lgals1, Lgals3, Lrrc8c, Nabp1, Pfkp, Scd2, Sem4a4, Syk

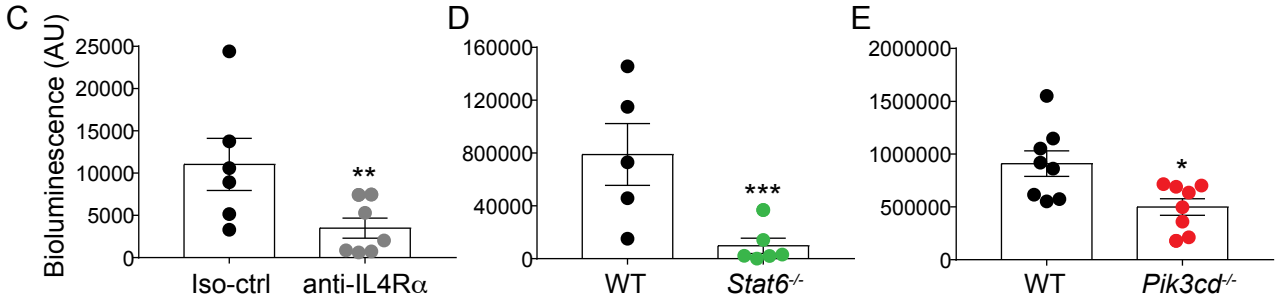

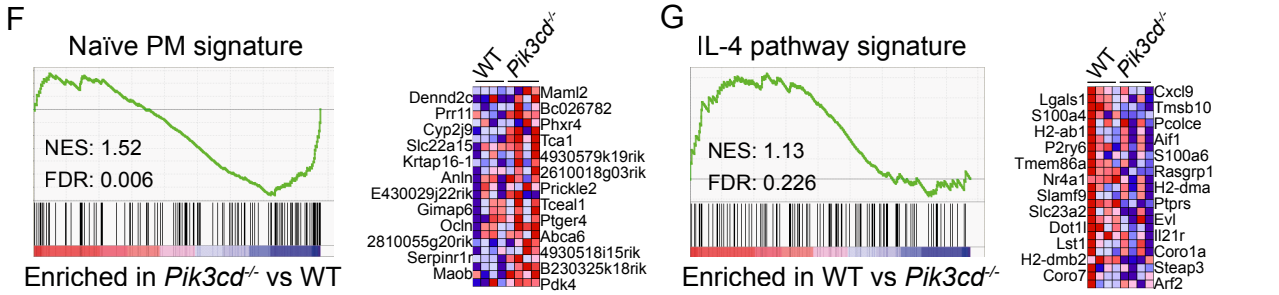

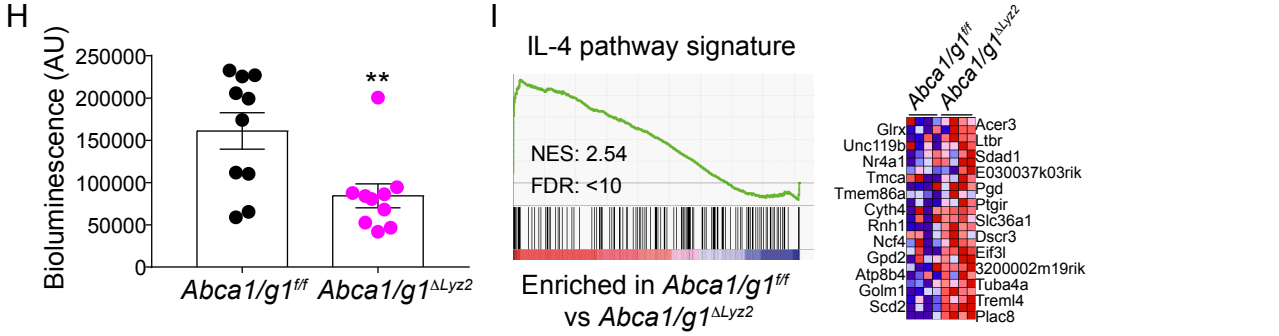

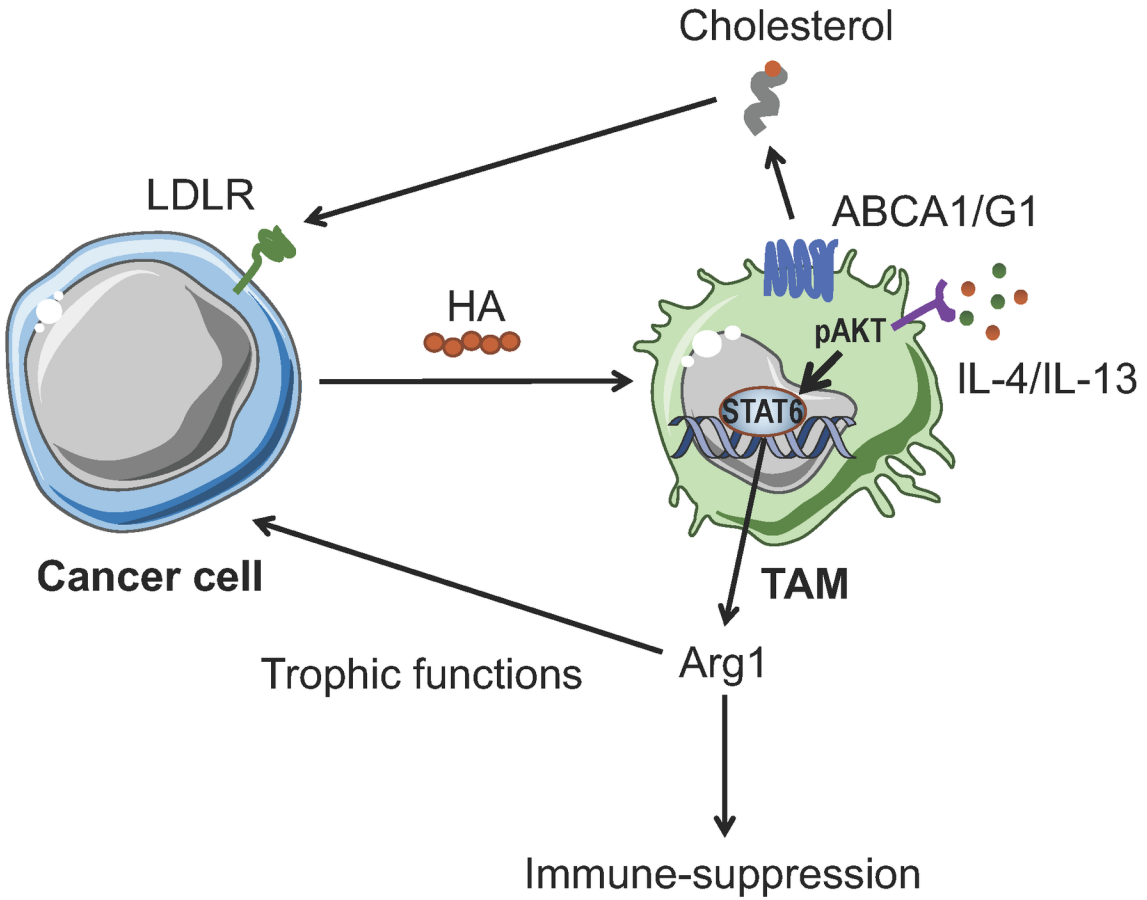
Cholesterol
LDLR
ABCA1/G1
HA
pAKT
IL-4/IL-13
STAT6
Cancer cell
TAM
Trophic functions
Arg1
Immune-suppression